3.1 Introduction

As discussed in chapter I, the crystal structure of $BiFeO_3$ is rhombohedral in the R3c space group [Jacobson et al. (1975); Fischer et al.(1980); Sosnowska et al. (2002)]. The crystal structure of BF-xPT solid solutions at room temperature is still controversial. The Morphotropic phase boundary (MPB) in the BF-xPT system has been traditionally believed to separate the stability fields of the rhombohedral and tetragonal phases in the R3c and P4mm space groups, respectively [Smith et al. (1968)]. Fedulov et al. [Fedulov et al. (1964)] have reported that the range of MPB was x=0.27 to 0.34 while on the other hand Woodward et al. [Woodward et al.(2003)] reported that the range of MPB was x=0.30 to 0.40. However, [Zhu et al. (2008)], it have been proposed that the MPB region extends from x=0.20 to x=0.40 giving an unusually large width $\Delta x=0.20$ for the MPB region in the BF-xPT system. It was also shown that in carefully prepared samples, the monoclinic and tetragonal phases are stable for x=0.27 and x=0.31, respectively [Bhattacharjee et al. (2007)], where as two phases coexist for $0.28 \leq x \leq 0.30$ composition range. The ceramic powder of BF-xPT prepared by mechanosynthesis process, the width of the MPB is shown to be $\Delta x=0.075$ [Correas et al. (2011)]. There is no satisfactory explanation till date as to why different workers report such widely differing values for the width of the MPB region ranging from $\Delta x=0.03$ [Bhattacharjee et al. (2011)] to $\Delta x=0.20$ [Zhu et al. (2008)]. The MPB in the magnetoelectric multiferroic BF-xPT is also dependent on crystallite size. Kothai et al. [Kothai et al. (2013), (2014)] have reported a MPB region depending on different crystallite size, however for the nanoparticles the crystal structure has been reported to be rohmbohedral for 71BFPT powder [Narayan et al.(2017)].

In this chapter, we attempt to resolve the existing controversies regarding the crystal structures of BF-xPT at room temperature from a systematic structural study using Rietveld analysis of high resolution synchrotron x-ray diffraction (SXRD) data for the compositions =0.5 and x=0.25, on the both side of MPB for both bulk and nano particles. Laboratory x-ray diffraction data are used for the structural analysis of the BF-xPT powder, which is calcined at 550℃ ($0.2<x\leq0.5$). A brief introduction to the Rietveld refinement technique is also included in this chapter.

3.2 Experimental

For x-ray characterizations, the sintered pellets were crushed to fine powders and then annealed to remove the strains introduced during crushing. Synchrotron x-ray diffraction (SXRD) patterns were collected at high resolution powder diffraction beamline P02.2 at PETRAIII, DESY, Hamburg, Germany for resolving the controversy about the structure. The wavelength for the synchrotron x-ray diffraction used was0.2079 Å (60 keV). The samples were kept inside Kapton tubes having diameter of 1.0 mm with a total $\mu R<1$.

The BF-xPT powder, which is calcined at 550℃ ($0.2<x\leq0.5$) are characterized by X-ray diffraction measurements using an 18 kW rotating anode (CuKα) based Rigaku (RINT 2000/ PC series) powder diffractometer operating in the Bragg- Brentano geometry and fitted with a graphite monochromator in the diffracted beam. The operating voltage and current were kept at 40 kV and 150 mA, respectively.

3.3 A brief introduction of Rietveld refinement method

The method of finding the arrangement of atoms within a crystal system is known as X-ray crystallography, in which a beam of x-rays is diffracted by a crystal in specified directions. From the intensities and angles of these diffracted beams, the mean positions of the atoms in the crystal can be determined. For the new materials, single crystal x-ray

diffraction is commonly used to find out the structures. However, there is some limitation of this technique by which the ability to grow nearly perfect crystals that are suitable for diffraction. Due to this limitation and the time and costintensive nature of the technique, structural characterization using x-ray powder diffraction is more common.

Dr. H. Rietveld was the first, who have carried out a computer program to make use of the full information content of the powder diffraction pattern which is now commonly known as the 'Rietveld refinement', or 'Rietveld analysis' or 'Rietveld method'. This is a least squares refinement method in which the refinements are carried out until the best fit is obtained between the entire observed powder diffraction pattern taken as a whole and the entire calculated pattern based on the simultaneously refined model for the crystal structure, diffraction optics effect, instrumental factors and other specimen characteristics [Young (1996)]. The parameter which is sought to be minimized is the residual, Sy:

$$S_y = \sum_i w_i \, (y_{oi} - y_{ci})^2 \ldots\ldots\ldots\ldots\ldots\ldots (3.1)$$

where, y_{oi} is the observed and y_{ci} is the calculated intensity at the i^{th} step and w_i is a suitable weight given by $(w_i)^{-1} = y_{oi}$.

A powder diffraction pattern results from several individual reflection, each of which has a peak height, a peak position, a breadth, tails which decay gradually with distance from the peak position, and an integrated area which is proportional to the Bragg Intensity Ik of each reflection where k stands for the Miller indices h,k,l. The intensity Ik is proportional to the square of the structure factor ($I_k \alpha |F_k|^2$) [Young (1996)]. Typically, many Bragg reflections contribute to the intensity, y_i, observed at any arbitrarily chosen point 'i' in the powder diffraction pattern. The calculated intensities y_{ci} are determined from the $|F_k|^2$

values calculated from the proposed structural model by summing up the calculated contributions from the neighbouring Bragg reflections plus the background:

$$y_{ci} = s \sum L_k |F_k|^2 \Phi(2\theta_i - 2\theta_k) P_k A + y_{bi} \ldots\ldots\ldots\ldots\ldots\ldots\ldots (3.2)$$

where s is the scale factor, k represents the Miller indices, h, k, l, for a Bragg reflection, L_k contains the Lorentz, polarization, and multiplicity factors, Φ is the reflection profile function, P_k is the preferred orientation function, A is an absorption factor, F_k is the structure factor for the k^{th} Bragg reflection, and y_{bi} is the background intensity at the i^{th} step [Young (1996)]. The Rietveld technique is a structure refinement technique where the knowledge of the basic structure is required in advance. In recent years, however, attempts have been made to solve unknown structures also using this technique [Peuchart et al. (1998)]. The shape of a powder diffraction reflection is influenced by both the sample (e.g. domain, size, stress/strain, defects) and the instrument (e.g. radiation source, geometry, slit sizes), and they vary as a function of 2θ. Among the various peak shape functions, the pseudo-Voigt, an approximation of the Voigt function, is most widely used. The pseudo-Voigt (pV) function is simply a linear combination of Lorentzian (L) and Gaussian (G) components in the ratio [Young (1996)]

$$pV = \eta L + (1-\eta)G \ldots\ldots\ldots\ldots\ldots\ldots (3.3)$$

Where, η is the pseudo-Voigt mixing parameter. All peak shape functions contain half width of the Bragg peaks or the full width at half maxima (FWHM) whose angular dependence is expressed by the famous Coglioti function [Caglioti et al. (1958)]:

$$(FWHM)^2 = U\tan^2\theta + V\tan\theta + W \ldots\ldots\ldots\ldots\ldots\ldots (3.4)$$

Where, U, V and W are half width parameters.

The parameters which are refined in the Rietveld method include structural parameters (positional coordinates, unit cell parameters and thermal parameters), sample parameters

(strains, domain size, preferred orientation), instrumental parameters (FWHM of the peaks due to diffraction geometry, shift of origin, background etc) and the scale factor.

Rietveld refinement process will adjust the refinable parameters until a 'best fit' for the entire calculated pattern to the entire observed pattern is obtained. It is important to check the adequacy of the selected structural model in giving global minima, rather than local ('false') minima, in the agreement factors. One needs various criteria of fit usually called agreement factors, in order to make these choices. The indicators used in the refinements are the various R-factors (or agreement factors) which are defined as follows [Young (1996)]:

(i) R- structure factor $:R_F=\frac{\sum|(I_K(obs'))^{\frac{1}{2}}-I_K(cal)^{\frac{1}{2}})|}{\sum(I_k(obs'))^{\frac{1}{2}}}$

(ii) R-profile factor $:R_p=\frac{\sum|y_{oi}-y_{ci}|}{\sum y_{oi}}$

(iii) R-Bragg factor $:R_B=\frac{\sum|I_K(obs')-I_K(cal)|}{\sum(I_k(obs'))}$

(iv) R-Weighted profile factor $:R_{wp}=\left\{\frac{\sum wi(y_i(obs)-y_i(cal))}{\sum w_i(y_i(obs))^2}\right\}^{1/2}$

(v) R-expected weighted profile factor $:R_{exp}=\left[\frac{(N-P)}{\sum w_i y2_{oi}}\right]^{1/2}$

In the above expressions IK is the intensity assigned to the K_{th} Bragg reflection at the end of the refinement cycles. N and P are number of observations and variables. The Bragg intensity IK is rarely observed directly. Therefore the IK values in the expression for RF and RB are obtained from the total observed intensity using programmatic allocation which is generally biased towards the structural model being refined.

The goodness -of- fit indicator 'S' is

$$S=\frac{R_{WP}}{R_e}=\left[\frac{S_y}{(N-P)}\right]^{1/2} \ldots\ldots\ldots\ldots\ldots\ldots (3.5)$$

The S value depends on the quality of powder diffraction data and is only an indicator of the global minimum solution. Irrespective of the S value, one seeks to achieve a difference profile as flat as possible before accepting a model. The goodness of fit of the system is also represented by an indicator called χ^2 and expressed as

$$\chi^2 = S^2 = \left[\frac{R_{wp}}{R_{exp}}\right]^2 = \left[\frac{S_y}{(N-P)}\right] \ldots\ldots\ldots\ldots\ldots\ldots (3.6)$$

From purely mathematical point of view, RWP is the most meaningful among all the agreement factors.

3.4 Rietveld refinement details of BF-xPT

Rietveld refinements were carried out using the FULLPROF package [Carvajal (2008)]. The Wyckoff positions and the asymmetric unit for the various space groups used during the Rietveld refinements of different crystallographic phases of BF-xPT system in the present work are given below:

1. For the rhombohedral phase with the R3c space group, we used hexagonal axes with lattice parameter $a_H = b_H = \sqrt{2}a_R$ and $c_H = 2\sqrt{3}a_R$, where a_R represents the rhombohedral cell parameter. There are three ions (Bi^{3+}/ Pb^{2+}, Fe^{3+}/Ti^{4+} and O^{2-}) in the asymmetric unit of the rhombohedral structure. The Bi^{3+}/ Pb^{2+} and Fe^{3+}/Ti^{4+} ions occupy the 6(a) Wyckoff site at (0, 0, z) while on the other hand O^{2-} ions at the 18(b) Wyckoff sites at (x, y, z). As per Megaw et al. (1975), the coordinates of all the atoms in the asymmetric unit cell of the R3c space group can also be written as a function of the displacement parameters s, t, d and e : Bi^{3+}/ Pb^{2+} (0.0, 0.0, 0.25+s), Fe^{3+}/Ti^{4+} (0, 0, t), O^{2-} (0.1666-2e-2d, 0.3333-4d, 0.0833). The ‘s’ and ‘t’ parameters describe the polar displacement of cations Bi^{3+}/ Pb^{2+} and Fe^{3+}/Ti^{4+}

along $[111]_{rh}$. The displacement parameter 'e' of oxygen (O^{2-}) from its ideal cubic position is related to the tilt angle (ω) of antiphase rotation of the oxygen octahedra about the trigonal $[111]_{rh}$ or $[001]_h$ direction through the expression $\omega = \tan^{-1}(4e\sqrt{3})$ Megaw et al. (1975). The parameter'd' is related to the distortion of the BO_6 (B: Fe^{3+}/Ti^{4+}) octahedra.

2. The asymmetric units of the monoclinic space groups Cc predicted by ISOTROPY [Stokes et al]. There is only one Wyckoff site symmetry 4(a) with the asymmetric unit of the structure consisting of five atoms.

   Bi^{3+}/Pb^{2+} :(0.00, 0.25, 0.00), Fe^{3+}/Ti^{4+}: (0.25 +δx, 0.25 + δy, 0.75 + δz)

   O1: (0.00+ δxO_1, 0.25 + δyO_1, 0.50 + δzO_1)

   O2: (0.25 + δxO_2, 0.50 + δyO_2, 0.00 + δzO_2)

   O3: (0.25 + δxO_3, 0.00 + δyO_3, 0.00 + δzO_3)

3. The asymmetric units of the monoclinic with space groups Ic is given as

   Bi^{3+}/Pb^{2+} :(0.00, 0.00, 0.00), Fe^{3+}/Ti^{4+}: (0.5 +δx, 0.00, 0.00 + δz)

   O1: (0.5+ δxO_1, 0.00, 0.00 + δzO_1)

   O2: (0.0 + δxO_2, 0.0 + δyO_2, 0.0 + δzO_2)

   O3: (0.5 + δxO_3, 0.5 + δyO_3, 0.0 + δzO_3)

4. In tetragonal phase with P4mm space group, Bi^{+3}/Pb^{+2} ions occupy 1(a) sites at (0,0,δz), Fe^{+3}/Ti^{+4} occupy 1(b) sites at (0.5,0.5,0.5+δz). The three oxygen atom in the symmetric unit of the perovskite cell occupy two different Wyckoff positions: 1(b) site at (0.5, 0.5, δz) and 2(c) site at (0.5, 0, 0.5+δz). Taking Pb/Bi at the origin, the atomic positions can be described in terms of three parameters δz_B, δz_{OI} and δz_{OII} only, where δz_B stands for the z coordinates for the B site, i.e. Fe^{3+}/Ti^{4+}

cation. Thus the coordinates of the asymmetric unit used in the refinements are [Shirane et al. (1956)]:

Bi^{3+}/ Pb^{2+}: (0, 0, 0), Fe^{3+}/Ti^{4+}: (0.5, 0.5, 0.5 + δz_B), O1 : (0.5,0.5, δzO_I) and

O2 :(0.5, 0, 0.5+ δzO_{II}).

5. For the cubic phase in the Pm3m space group, there are three ions (Bi^{3+}/ Pb^{2+}, Fe^{3+}/Ti^{4+}, $O_I^{2-}$and O_{II}^{2-}) in the asymmetric unit with Bi^{3+}/ Pb^{2+} ions occupying 1(a) site at (0, 0, 0), Fe^{3+}/Ti^{4+} (b) site at (0.5, 0.5, 0.5) and O^{2-} at 3(c) sites at (0.5, 0.5, 0).

3.5 Results and discussion

3.5.1 Rietveld refinement of the structure of BF-xPT for x=0.5

The tetragonal phase in BF-xPT system persists over a large composition range starting from PT (x=1) end up to x=0.31 [Bhattacharjee et al (2010)]. One of the most interesting features of the tetragonal phases of BF-xPT is that the tetragonality goes on increasing with decreasing PT ($PbTiO_3$) content upto x=0.31. For the other solid solution systems in which MPB is present, shows their tetragonality decreases with decreasing PT content like (1-x)$BiMnO_3$-x$PbTiO_3$ [Woodward et al. (2004)] and (1-x)$BiScO_3$-x$PbTiO_3$ [Chaigeneau et al. (2007)].

The structure of tetragonal phase of BF-xPT powder have been refined by many researcher like Chen et al (2006), Ranjan et al (2010), Bhattacharjee et al (2010), etc. We have refine SXRD data obtained for the all sizes of BF-0.50PT powder (as discussed in chapter II). The 120 nm size powder which is sintered at 1050℃ shows clear splitted peaks of tetragonal phase as like bulk sample earlier reported by Bhattacharjee et al (2010). The 18 nm size powder , which is calcined at 550℃, shows cubic like XRD pattern. Now our objective is to investigate the real crystal structure of this nano sized

powder using SXRD data. Fig. 3.1 shows the elaborate scheme which was adopted to fit the SXRD data of 18 nm particle size. The SXRD data indicates that the sample has got a cubic structure. The Rietveld fit with single phase cubic Pm3m space group, however leads to rather poor fit with very high χ^2 value (101.9) (see Fig. 3.1a).

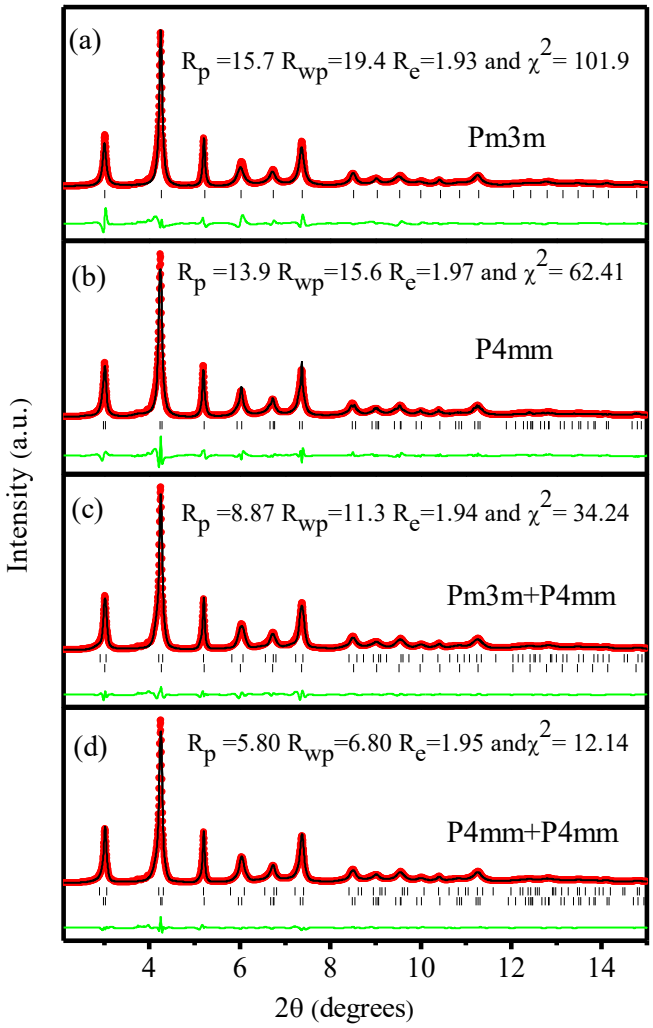

Fig 3.1 Rietveld fit of synchrotron X-ray powder diffraction pattern of BF-0.50PT powder of 18 nm particle size using different structural models.

The asymmetric broadening towards lower 2θ angle of the 200 and 220 pseudocubic peaks suggests that the structure may have lower symmetry than cubic. Accordingly, we considered the tetragonal space group P4mm for refinement. While this led to considerable improvement in χ^2 which changed from 101.9 to 62.41, the χ^2 value is still large (Fig. 3.1b). At this stage, we considered Rietveld refinement using coexistence of tetragonal and cubic phases which led to further improvement in χ^2(from 62.41 to 34.24) but still the fits are not good (Fig.3.1c). Finally, we attempted to fit the diffraction data with two tetragonal phases with different tetragonalities but the same space group (P4mm). This led to the best possible fit shown in Fig 3.1(d) with significantly improved χ^2 values (12.14). This indicates that the samples having average particle size of 18 nm consist of two coexisting tetragonal phases with different tetragonalities. Rietveld refinements for the different size powders confirmed that the 120 nm powder consists of a single tetragonal phase, whereas all the smaller size powders contain two coexisting tetragonal phases which is shown in fig.3.2. The (002) peak which is clearly shown in fig.3.2 (a), is shifted towards higher angle with decreasing size and it disappears for 18 nm size powder. The refined parameters of various sizes of BF-0.5PT are listed in Table1. The variation of lattice parameters, cell volume of the various sizes is shown in fig. 3.3(a), which clearly indicates that as size reduces its lattice constant decreases gradually. The tetragonality (c/a-1) of bulk BF-0.5PT sample is around 14.16% which is significantly larger as compared to that of $PbTiO_3$ at room temperature (~6%). On the other hand, the tetragonality of nano-powders is reduced to ~5.75% which is approximately same of pure $PbTiO_3$, fig. 3.3 (b). We have shown that nano-BF-0.5PT powder consists of core-shell type structure with different tetragonalties in core and shell region of each particle [will be

discuss in next chapter]. It is obvious that bulk sample consists ~100% T_1 phase i.e. core type structure.

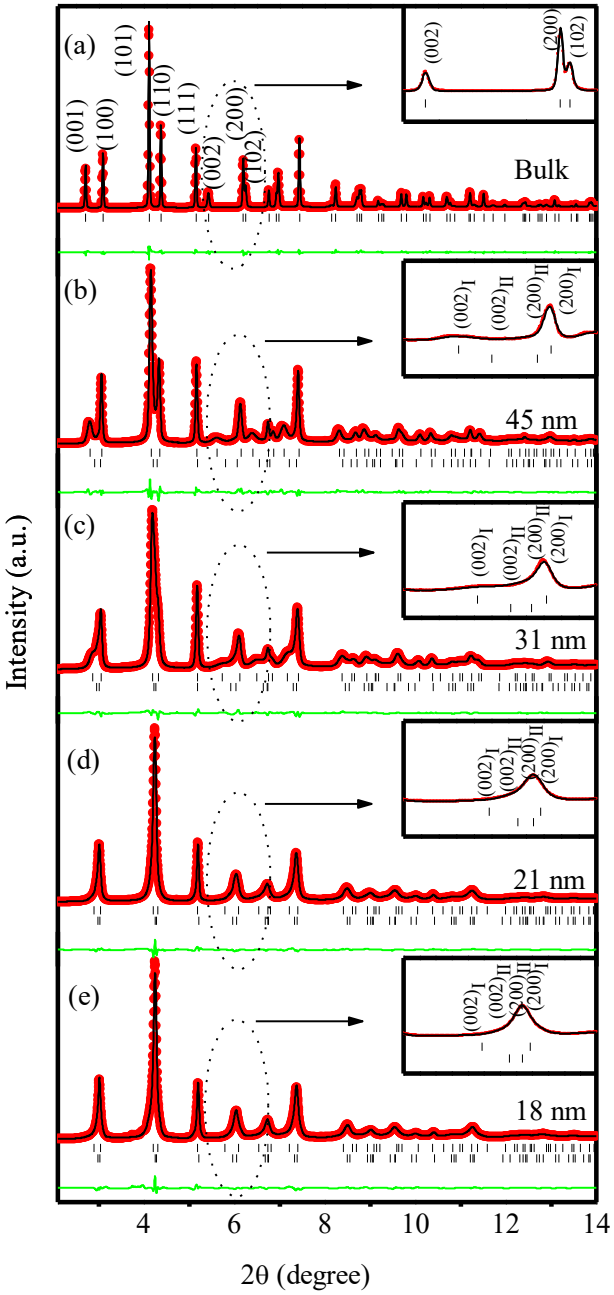

Fig 3.2 Synchrotron High resolution x-ray diffraction pattern of BF-0.5PT powder with varying sizes.

Table 3.1: Details of Rietveld fitting parameters for SXRD pattern of BF-0.50PT sample having different particle size.

BF0.5PT with different sizes		Fractional coordinates				Thermal Parameters ($Å^2$)	Lattice Parameters (Å)	Statistical parameters
		Atom	x	y	z			
18 nm	Tetragonal phase-1	Bi/Pb	0.0	0.0	0.0	$\beta_{11}=\beta_{22}=0.032(1),\beta_{33}=0.0064(4)$	a=b=3.91261(7) c=4.13617(5)	R_p= 5.80 R_{wp}= 6.80 R_{exp}= 1.95 χ^2 = 12.14
		Fe/Ti	0.5	0.5	0.568(4)	B_{iso}=1.003(2)		
		O_1	0.5	0.5	0.129(1)	$\beta_{11}=\beta_{22}$= 0.212(5), β_{33}=0.51(0)		
		O_2	0.0	0.5	0.655(1)	β_{11}= 0.010(1), β_{22}=0.015(9), β_{33}= 0.19(5)		
	Tetragonal phase-2	Bi/Pb	0.0	0.0	0.0	$\beta_{11}=B_{22}$=0.078(3),β_{33}= 0.031(1)	a=b=3.94988(8) c=4.00117(54)	
		Fe/Ti	0.5	0.5	0.518(1)	B_{iso}= 0.982(1)		
		O_1	0.5	0.5	0.130(6)	$\beta_{11}=\beta_{22}$= 0.014(1), β_{33}=0.0008(1)		
		O_2	0.0	0.5	0.580(4)	β_{11}= 0.019(3), β_{22}= 0.013(2), β_{33}= 0.002(5)		
21 nm	Tetragonal phase-1	Bi/Pb	0.0	0.0	0.0	$\beta_{11}=\beta_{22}$= 0.033(1),β_{33}= 0.003(3)	a=b= 3.91766(8) c= 4.1212(1)	R_p= 5.35 R_{wp}= 6.14 R_{exp}= 1.66 χ^2 = 13.75
		Fe/Ti	0.5	0.5	0.552(5)	B_{iso}= 0.333(5)		
		O_1	0.5	0.5	0.115(9)	$\beta_{11}=\beta_{22}$= 0.177(7),β_{33}= 0.012(5)		
		O_2	0.0	0.5	0.649(1)	β_{11}= 0.035(2), β_{22}= 0.155(7), β_{33}= 0.10(1)		
	Tetragonal phase-2	Bi/Pb	0.0	0.0	0.0	$\beta_{11}=\beta_{22}$= 0.082(1),β_{33}= 0.027(8)	a=b= 3.95015(6) c= 4.0029(4)	
		Fe/Ti	0.5	0.5	0.549(7)	B_{iso}=1.91(6)		
		O_1	0.5	0.5	0.080(3)	$\beta_{11}=\beta_{22}$= 0.061(4),β_{33}= 0.063(8)		
		O_2	0.0	0.5	0.568(1)	β_{11}= 0.017(6), β_{22}= 0.051(9), β_{33}= 0.042(2)		
31 nm	Tetragonal phase-1	Bi/Pb	0.0	0.0	0.0	$\beta_{11}=\beta_{22}$= 0.038(2),β_{33}= 0.004(9)	a=b= 3.90100(0) c= 4.16010(1)	R_p= 5.14 R_{wp}= 6.44 R_{exp}=1.57 χ^2 =16.8
		Fe/Ti	0.5	0.5	0.560(3)	B_{iso}= 0.16(6)		
		O_1	0.5	0.5	0.129(8)	$\beta_{11}=\beta_{22}$= 0.019(6),β_{33}= 0.10(5)		
		O_2	0.0	0.5	0.628(1)	β_{11}= 0.032(3), β_{22}= 0.047(8), β_{33}= 0.09(4)		
	Tetragonal phase-2	Bi/Pb	0.0	0.0	0.0	$\beta_{11}=\beta_{22}$= 0.060(1),β_{33}= 0.069(8)	a=b= 3.95334(9) c= 4.0281(2)	
		Fe/Ti	0.5	0.5	0.513(6)	B_{iso}= 1.20(9)		
		O_1	0.5	0.5	0.104(8)	$\beta_{11}=\beta_{22}$= 0.021(6),β_{33}= 0.073(6)		
		O_2	0.0	0.5	0.632(6)	β_{11}= 0.037(2), β_{22}= 0.031(3), β_{33}= 0.07(2)		
45 nm	Tetragonal phase-1	Bi/Pb	0.0	0.0	0.0	$\beta_{11}=\beta_{22}$= 0.031(5),β_{33}= 0.026(0)	a=b= 3.88060(1) c= 4.25320(1)	R_p=6.33 R_{wp}=7.45 R_{exp}=1.63 χ^2 = 21.0
		Fe/Ti	0.5	0.5	0.560(9)	B_{iso}= 0.74(0)		
		O_1	0.5	0.5	0.139(3)	$\beta_{11}=\beta_{22}$= 0.038(8),β_{33}= 0.055(1)		
		O_2	0.0	0.5	0.646(4)	β_{11}= 0.026(7), β_{22}= 0.053(4), β_{33}= 0.15(8)		
	Tetragonal phase-2	Bi/Pb	0.0	0.0	0.0	$\beta_{11}=\beta_{22}$= 0.045(9),β_{33}= 0.007(5)	a=b= 3.93167(4) c= 4.09467(8)	
		Fe/Ti	0.5	0.5	0.555(1)	B_{iso}= 0.22(9)		
		O_1	0.5	0.5	0.124(1)	$\beta_{11}=\beta_{22}$= 0.031(6),β_{33}= 0.037(6)		
		O_2	0.0	0.5	0.636(9)	β_{11}= 0.061(2), β_{22}= 0.065(3), β_{33}= 0.086(5)		
120 nm	Tetragonal phase-1	Bi/Pb	0.0	0.0	0.0	$\beta_{11}=\beta_{22}$= 0.026(3),β_{33}= 0.025(8)	a=b= 3.84852(7) c= 4.39351(1)	R_p=7.16 R_{wp}=8.56 R_{exp}=1.39 χ^2 =37. 65
		Fe/Ti	0.5	0.5	0.558(3)	B_{iso}= 0.36(2)		
		O_1	0.5	0.5	0.143(5)	$\beta_{11}=\beta_{22}$= 0.013(6),β_{33}= 0.031(4)		
		O_2	0.0	0.5	0.652(9)	β_{11}= 0.045(1), β_{22}= 0.016(3), β_{33}= 0.023(3)		

The phase fraction of core type structure decreases as size of sample decreases and phase fraction of shell type structure i.e. T_2 phase increases gradually. The18 nm sample consist ~62% T_2 and 38% T_1 phase whereas sample of ~31nm size consist approximately ~50% of both T_1 and T_2 phases, which is seen in fig. 3.3(c).

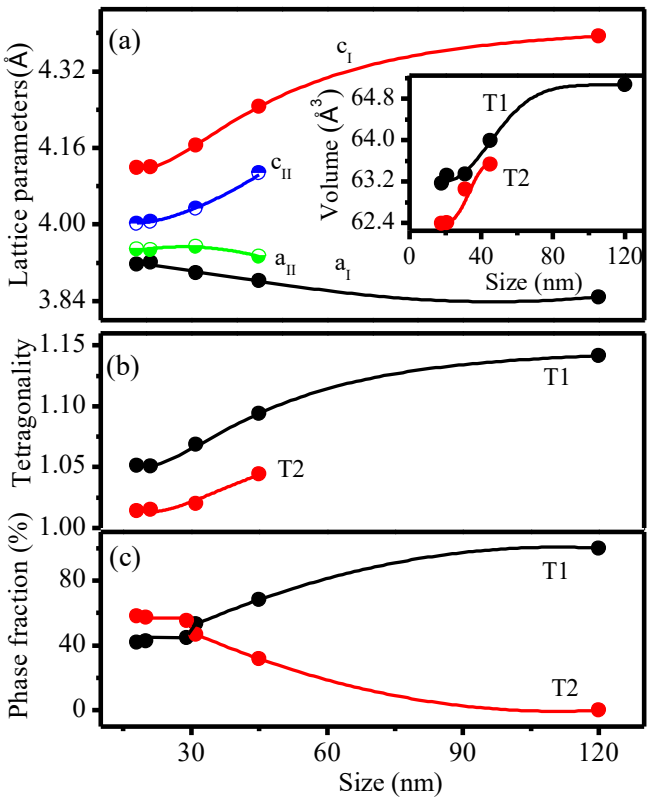

Fig.3.3 (a) Variation of lattice parameters and unit cell volume (inset) of tetragonal (T1and T2) with size obtained from Rietveld refinement (b) Variation of tetragonality and (c) phase fraction of tetragonal phase (T1and T2) with size.

3.5.2 Space group of BF-xPT for x=0.25

The XRD profiles of BF-0.25PT show the similar features to those expected for pure $BiFeO_3$, which include the presence of a characteristic superlattice reflection (311) due to the antiphase tilted oxygen octahedral in the unit cell. In recent years size reduction in pseudorhombohedral compositions of BF-xPT has been proposed to induce rhombohedral to tetragonal phase transition [Narayan et al (2017)]. However, the rhombohedral structure for the bulk BF-xPT in itself is controversial as both rhombohedral R3c and monoclinic Cc space groups have been proposed in the literature using laboratory source XRD data [Bhattacharjee et al (2010), Comyn et al. (2013), Smith et al .(1968), Ranjan et al. (2010),(2011), Sunder et al (1995)]. So there is a need to settle this controversy first using high resolution synchrotron x-ray diffraction (SXRD) data.

Fig.3.4 depicts the SXRD patterns of 200,220, 222 and 400 reflections of BF-0.25PT for different sizes for which the structure is monophasic. All the indices here are with respect to the doubled pseudocubic (pc) perovskite cell. The doublet nature of 220_{pc} and 222_{pc} pseudocubic (pc) profiles and singlet nature of 200_{pc} has been taken in the literature as proof of rhombohedral structure with R3c space group for BF-xPT with compositions on the BF end of the morphotropic phase boundary (MPB) in the earlier as well as some recent literature Ranjan et al. (2011), Kothai et al. (2013), (2014). However, this assignment of space group overlooks the anomalous peak broadening of h00 and hh0 peaks with respect to the hhh pseudocubic peaks as reported by Bhattacharjee et al (2010). For example, the ratio of the full width and half maximum (FWHM) of the 400_{pc} to the neighbouring peak of the 222_{pc} doublet is about1.62 for 2μm powder. Since these two peaks are neighbouring peaks, the change in their FWHM as a function of 2θ as per Caglioti function should be negligible but we find that 400_{pc} peak is much broader than

the individual peaks in the 222_{pc} profile [Caglioti et al (1958)]. A similar anomalous broadening has earlier been reported in the "rhombohedral" phase of PZT,PFN and PMN-x PT also, where it has been conclusively established by Rietveld refinement that this broadening cannot be modelled using anisotropic strain broadening and that the only way that the $h00_{pc}$, $hh0_{pc}$ and hhh_{pc} peaks can be fitted consistently is by lowering the symmetry from rhombohedral to monoclinic [Ragini et al. (2002), Singh et al. (2007), Singh et al. (2006), Stephens et al.(1999)]. Bhattacharjee and Pandey showed that the anomalous broadening of the $h00_{pc}$ (e.g. 200 in Fig.3) and $hh0_{pc}$ (e.g. 220 in Fig 3. Peaks of BF-xPT composition with $0.10 \leq x \leq 0.27$ (i.e. on the BF side of the MPB) cannot be accounted for in the Rietveld refinements using the R3c space group [Bhattacharjee et al.(2010)]. It was shown that $PbTiO_3$ substitution changes the space group symmetry of BF to Cc for which an excellent fit was obtained for $h00_{pc}$, $hh0_{pc}$ and hhh_{pc} peaks consistently.

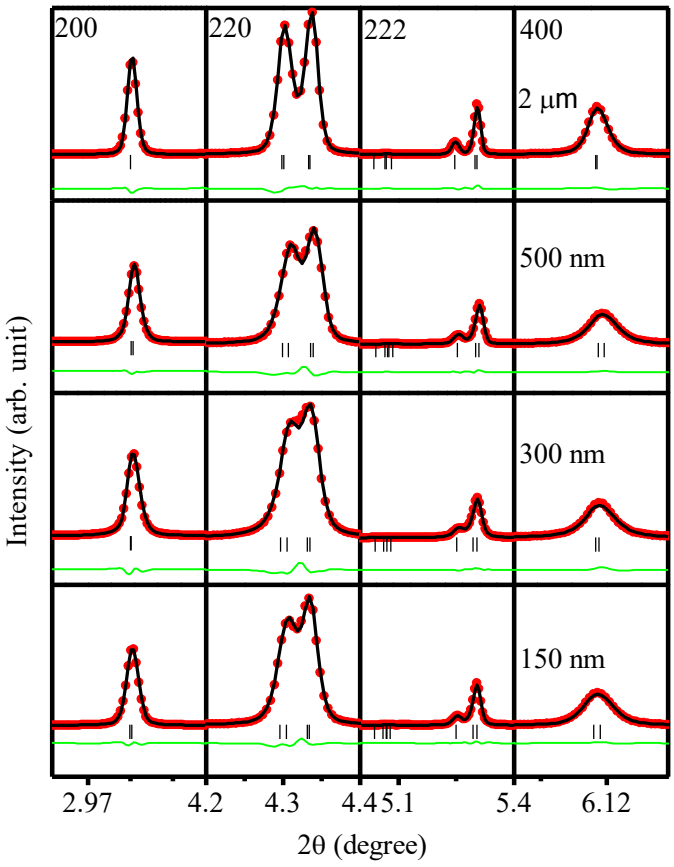

Fig. 3.4 Rietveld refinement profile for 200, 220, 222 and 400 psuedocubic reflections using Ic space group for BF-0.25PT.

However, the current literature continues to consider R3c space group for BF-xPT [Comyn et al. (2013), Ranjan et al. (2010), (2011)]. Since all these analyses were carried out using laboratory source XRD data, it is desirable to settle the structure of BF-0.25PT in the bulk and nanocrystalline forms using high resolution SXRD data first. Since the samples used in the present investigation were prepared by the sol-gel method, which is expected to ensure better chemically homogeneity as compared to the samples prepared by solid state diffusion route in the earlier work, it is expected that Rietveld analysis of high resolution SXRD data can resolve the controversy unambiguously [Zhu et al. (2004),(2008), Smith et al. (1968), Sunder et al.(1995)].

Accordingly, Rietveld refinements were carried out for both the R3c and Cc space groups. In the refinement, anisotropic strain broadening model of Stephen was used as a standard protocol for Rietveld refinements using SXRD data. The positional coordinates and the thermal parameters of all the atoms in the asymmetric unit were refined along with the unit cell parameters and various instrumental parameters. Fig. 3.5(a) compares the observed, calculated and difference profiles of a few selected pseudocubic reflections obtained by Rietveld refinement for the R3c and the Cc space groups for the 2μm size powder. It is evident from these figures that the fit for the R3c space group is rather bad for both the 200 and 220 pc reflections as compared to that for the Cc space group. Further, the fit is extremely poor for the 311 superlattice peak for the R3c space group as compared to the Cc space group. Further, there is a drastic decrease in goodness of fit χ^2 from 7.98 for the rhombohedral R3c space group to 1.5 for the monoclinic Cc space group. Thus both the χ^2 value as well as the quality of fit shown in Fig. 3.5(a) clearly rule out the rhombohedral R3c space group proposed in the earlier work and favours the Cc space group proposed by Shuvrajyoti and Pandey [Bhattacharjee et al. (2010)]. After settling the controversy about the rhombohedral R3c versus monoclinic Cc space group symmetries of BF-0.25PT using SXRD data for bulk powder (particle size 2μm), we also examined the possibility of the Cc space group reverting to R3c space group on decreasing the particle size.

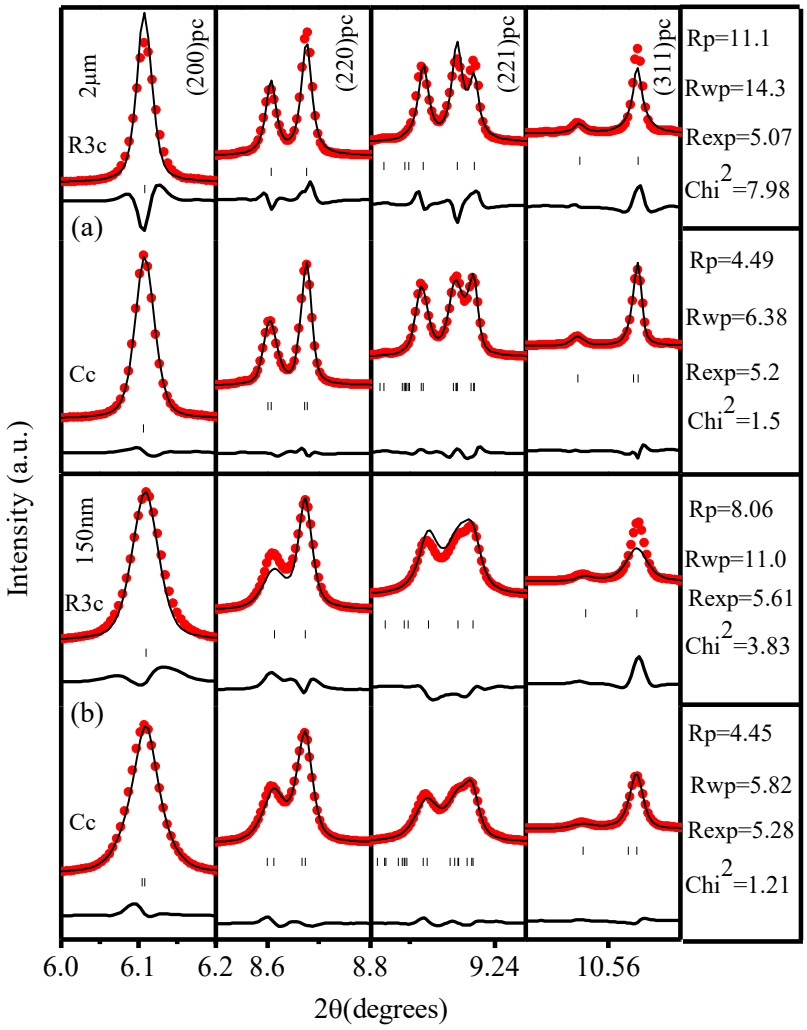

Fig. 3.5 Rietveld refinement profile for 200, 220, 221 and 311 psuedocubic reflections using R3c and Cc space group for (a) 2μm (b) 150 nm of BF-0.25PT.

Fig. 3.5 (b) depicts the fits for a few selected pseudocubic peaks of BF-0.25PT powders of ~150nm size. As in the case of bulk powder, the fits for Cc space group is evidently superior to the R3c space group for 150nm size powder. Table 3.2 lists the refined parameters of BF-0.25PT powders of different sizes. For the coordinates, we have used the equivalent Ic setting instead of the Cc setting, which is the non-standard setting of Cc, as the visualization of the superexchange pathways discussed in next chapter.

Table 3.2 Refined structural parameters of BF-0.25PTof different sizes using Ic space group obtained from synchrotron x-ray diffraction.

BF0.25PT at different sizes.	Fractional coordinates				Thermal Parameters (Å^2)	Lattice Parameters (Å)	Statistical parameters
	Atom	x	y	z			
150 nm	Bi/Pb	0.0	0.0	0.0	B_{iso}= 1.30(1)	a= 5.5258(6) b= 5.4775(4) c= 7.7698(6) β= 90.52(1)	Rp=5.30 Rwp=6.86 Rexp=5.39 χ^2=1.61
	Fe/Ti	0.551(6)	0.0	0.248 (7)	B_{iso}=0.51(1)		
	O1	0.60(6)	0.0	-0.03(4)	B_{iso}=0.03(0)		
	O2	0.2(1)	0.23(8)	0.17(4)	B_{iso}=0.3(0)		
	O3	0.81(8)	0.7(1)	0.21(4)	B_{iso}=0.6(0)		
300 nm	Bi/Pb	0.0	0.0	0.0	B_{iso}= 1.36(3)	a= 5.5243(8) b= 5.4755(2) c= 7.7724(5) β= 90.47(4)	Rp=5.63 Rwp=6.74 Rexp=5.38 χ^2= 1.57
	Fe/Ti	0.555(8)	0.0	0.23(6)	B_{iso}=0.5(1)		
	O1	0.59(6)	0.0	-0.03(6)	B_{iso}= 0.3(0)		
	O2	0.29(1)	0.26(6)	0.18(5)	B_{iso}= 0.4(0)		
	O3	0.80(1)	0.71(5)	0.18 (4)	B_{iso}= 0.3(0)		
500 nm	Bi/Pb	0.0	0.0	0.0	B_{iso}= 1.29(1)	a= 5.5225(2) b= 5.4712(3) c= 7.7635(7) β= 90.56(2)	Rp=5.25 Rwp=6.72 Rexp=5.88 χ^2=1.30
	Fe/Ti	0.55(2)	0.0	0.23(2)	B_{iso}=0.59 (5)		
	O1	0.60(6)	0.0	-0.03(5)	B_{iso}= 0.16 (0)		
	O2	0.2 (1)	0.26(5)	0.17(4)	B_{iso}= 0.3(0)		
	O3	0.8(1)	0.72(7)	0.20(5)	B_{iso}= 0.6(0)		
2 µm	Bi/Pb	0.0	0.0	0.0	B_{iso}= 1.35(2)	a= 5.5237(5) b= 5.4758(2) c= 7.7763(4) β= 90.63 (1)	Rp=4.67 Rwp=7.91 Rexp=5.35 χ^2=2.18
	Fe/Ti	0.55(1)	0.0	0.23(3)	B_{iso}=0.57(5)		
	O1	0.60 (6)	0.0	-0.03(6)	B_{iso}= 0.8(0)		
	O2	0.28(8)	0.23(7)	0.16(8)	B_{iso}= 0.3(0)		
	O3	0.83(8)	0.75(8)	0.23(6)	B_{iso}= 0.5(0)		

In the context of tetragonal phase of BF-50PT, we have earlier discuss in this chapter, that the nanoparticles have a two tetragonal phases with different tetragonality. To verify this possibility for the monoclinic phase, we also carried out two phase Rietveld refinements for various possible core and the shell structures for the BF-0.25PT sample having lowest particle size (~150 nm), as this size is most susceptible for such a core-shell structure. Fig.3.6 depicts the Rietveld fits along with the χ^2 values the following possibilities: Cc (core)+Cc (shell), Cc (core)+R3c (shell) and Cc (core) + P4mm (shell)and R3c + P4mm.Refinements using these combinations of phases did not improve the fits as compared to single phase Cc. In fact, two-phase refinements invariably led to higher χ^2

values as compared to single-phase refinement using Cc space group. Normally χ^2 should decrease as the number of refinable parameters increases. However, in the present case the inclusion of second phase led to higher χ^2.

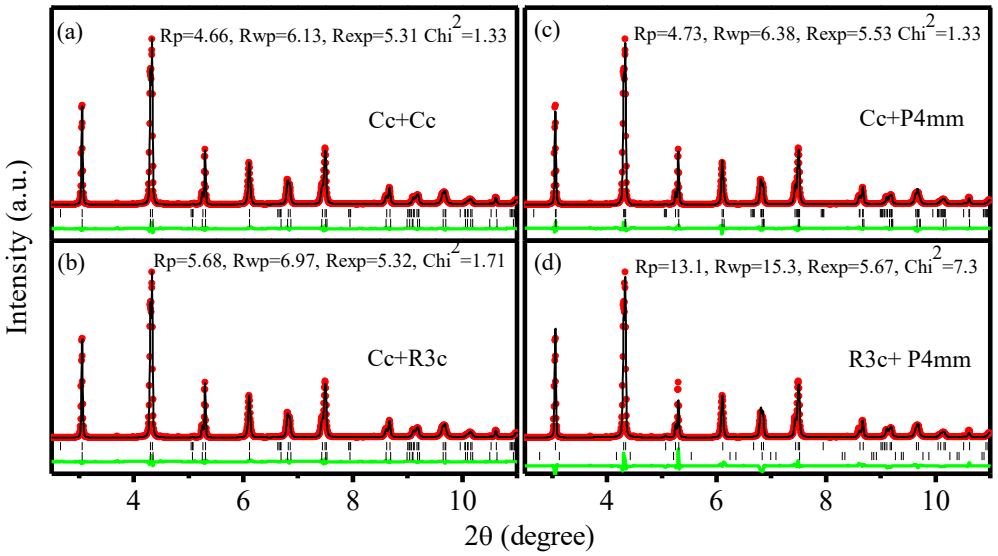

Fig. 3.6 Comparison of Rietveld refinement profile for four different structural models for BF-0.25PT.

3.5.3 Effect of particle size on the composition width of the phase coexistence region

Kothai et al.(2014) have reported that BF-xPT transform from a pure tetragonal phase to a state comprising tetragonal and rhombohedral phases as the average crystallite size is reduced from ~10 to ~1 μm, which means that smaller size crystalline powder have higher surface energy that creates an equivalent compressive stress to drives the system towards tetragonal-rhombohedral criticality. However, Bhattacharjee et al has already established that the rhombohedral symmetry of $BiFeO_3$ in R3c space group gets reduced to monoclinic in Cc space group as result of $PbTiO_3$ substitution. This monoclinic phase is stable in composition range of $0.1 \leq x \leq 0.27$ [Bhattacharjee et al.(2007)]. We have

calcined our samples at 550˚C which is lowest temperature for the synthesis of pure BF-x PT ($0.2<x\leq0.5$) powder, as discussed in chapter II. The size of powder gradually increases as substitution of $PbTiO_3$ in $BiFeO_3$. The particle sizes of these compositions are also listed in tables (2.1-2.7) in chapter II.

[Bhattacharjee et al.(2010)] have reported that stability of various crystallographic phases of BF-xPT as a function of composition. According to him, the compositions of BF-0.20PT and BF-0.25PT must be monoclinic, whereas the composition of BF-0.3PT have both tetragonal and monoclinic phase. In context with that, we have already established that the BF-0.25PT powder shows monoclinic phase even after reduction of size in the previous section of this chapter. [Bhattacharjee et al.(2011)] have reported MPB region leading to an extended from $\Delta x = 0.03$ for annealed samples to $\Delta x = 0.17$ for the stressed samples toward the $BiFeO_3$ richer side.

But in our case there is no significant change during crushing of sample. Fig.3.7, compare the x-ray diffraction profiles of uncrushed and crushed powders of a monoclinic compositions i.e. BF-0.20PT.

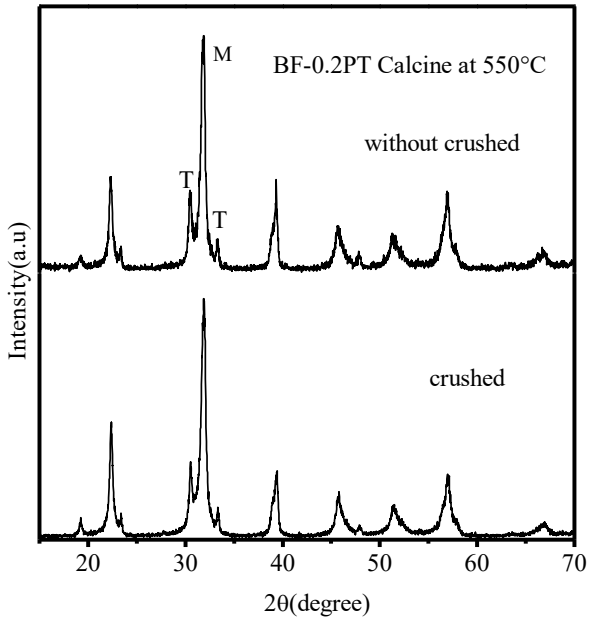

Fig.3.7 Room temperature x-ray powder diffraction profile of uncrushed and crushed powder of BF-0.20PT calcined at 550℃.

The new phase marked with (T) even present with main perovskite peak (M) before crushing the powder.

So, to confirm quantitatively the appearance of (T) tetragonal phase, we carried out Rietveld refinement for the calcined powders of BF-x PT with x=0.2, 0.25,0.30, 0.35 and 0.40. Fig. (3.8-3.10) depicts the calculated, observed and difference profiles of calcined powder. The calcined powder shows two phase structure model with value of χ^2=1.71, 1.62, 1.63 for BF-0.2PT, BF-0.25PT and BF-0.30PT respectively. The goodness of fit between the observed and calculated profile confirms that sample consist both monoclinic and tetragonal phase as predicted for monoclinic and tetragonal phase on MPB region [Bhattacharjee et al.(2007)] at room temperature. We have considered isotropic thermal parameters led to reasonable fit.

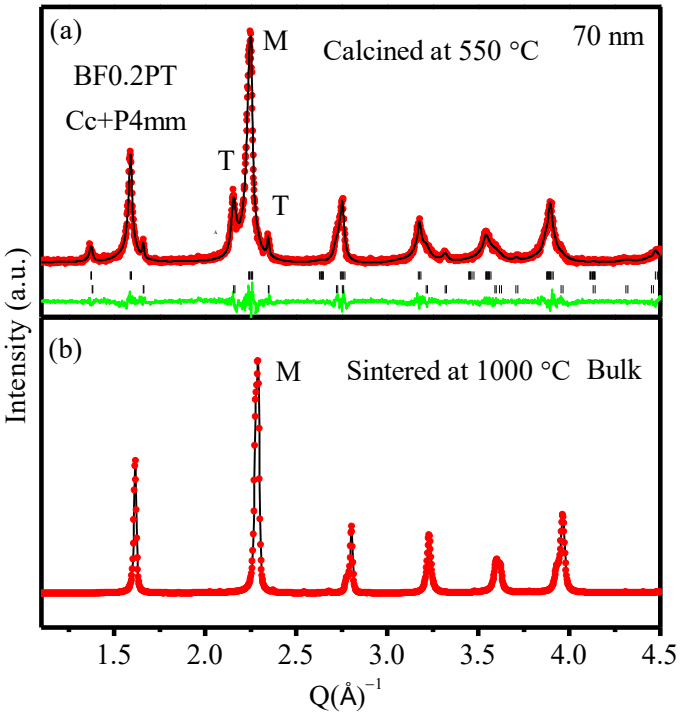

Fig.3.8 (a) Rietveld refinement profile of calcined BF-0.20PT powder (b) synchrotron x-ray powder diffraction pattern of bulk BF-0.20PT.

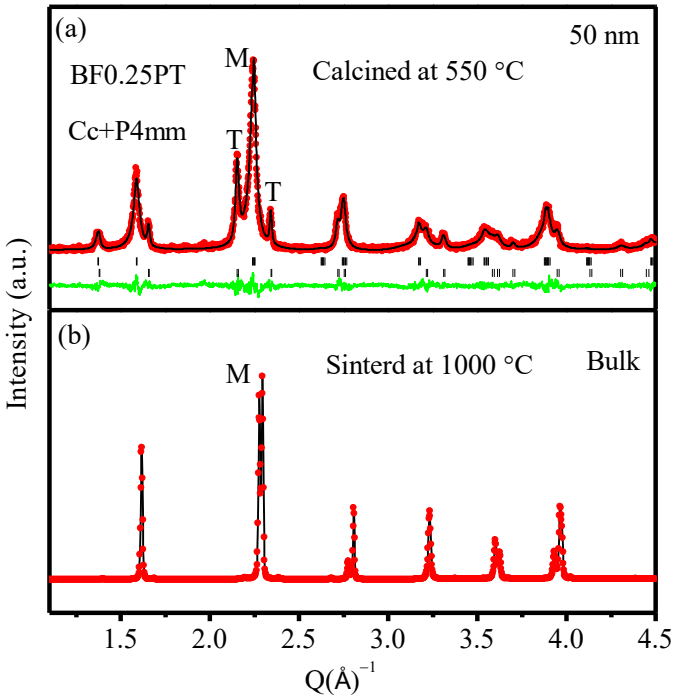

Fig.3.9 (a) Rietveld refinement profile of calcined BF-0.25PT powder (b) synchrotron x-ray powder diffraction pattern of bulk BF-0.25PT.

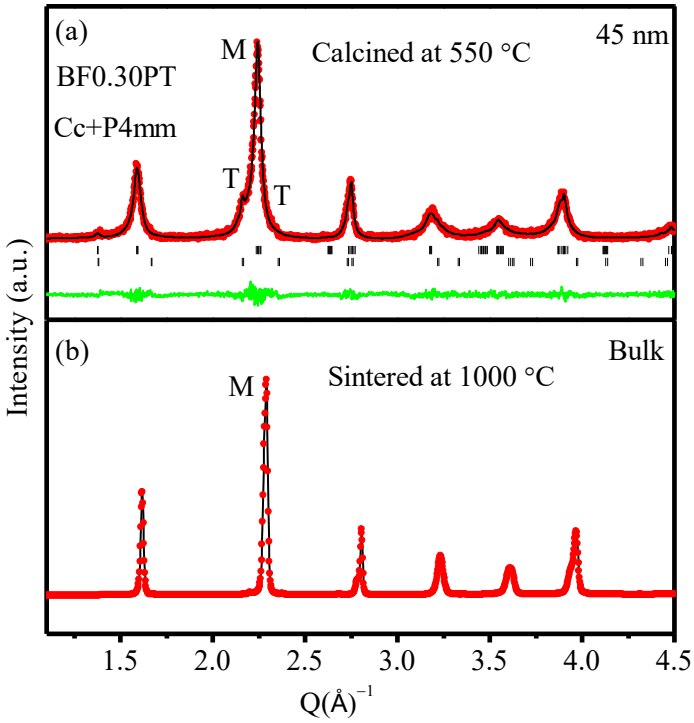

Fig.3.10 (a) Rietveld refinement profile of calcined BF-0.30PT powder (b) synchrotron x-ray powder diffraction pattern of bulk BF-0.30PT.

On the other hand sintered sample shows sharp and splited peaks, which confirms the crystallinity of samples. Fig.3.11 shows different structural models used to fit BF-0.35PT sample. We have considered that is it possible that monoclinic phase still present in sample, so we used monoclinic and tetragonal phases to fit it. The fitting between observed and calculated profile is rather unsatisfactory with χ^2=1.93.

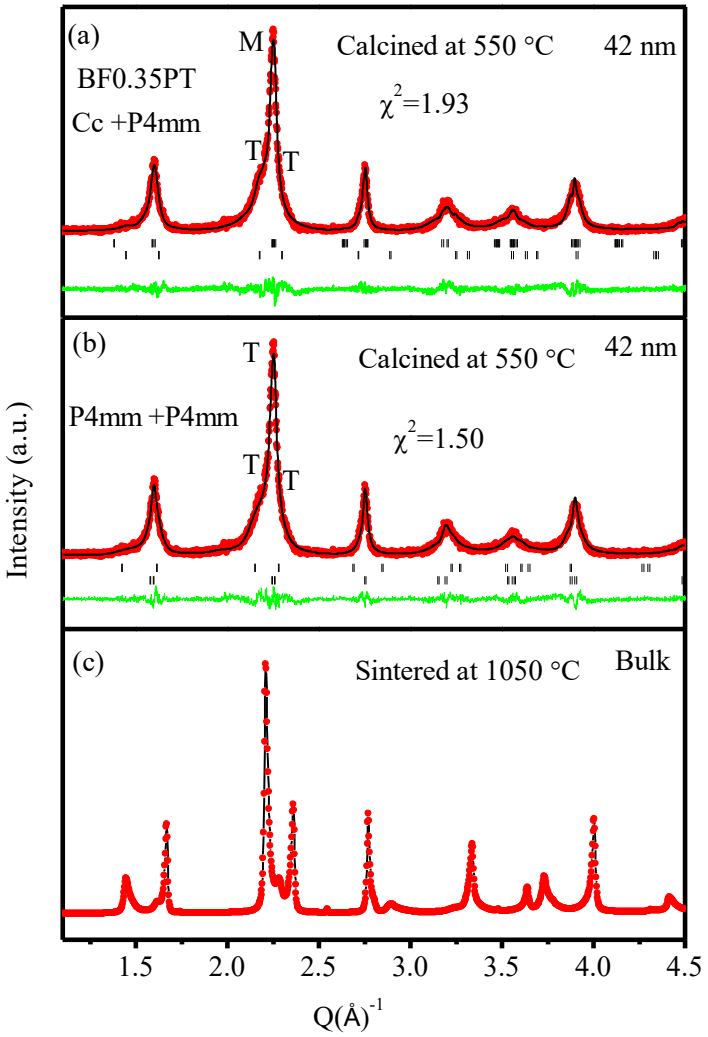

Fig.3.11 (a-b) Rietveld refinement profile of calcined BF-0.35PT powder with different model (c) synchrotron x-ray powder diffraction pattern of bulk BF-0.35PT.

As next step we considered coexistence of tetragonal (P4mm) and tetragonal (P4mm) phases in the Rietveld refinements. The fitting between observed and calculated profiles has improved a little with lower χ^2 value (1.50) as compared to that of (1.93) for P4mm and Cc space group. On the other hand BF-0.40PT is just close to the composition of BF-0.5PT, which show two tetragonal phases required to get best fit. So on behalf this conclusion we try to fit BF-0.4PT with two tetragonal phases. Fig. 3.12 shows that the

fitting between observed and calculated profile gives best fit with χ^2=1.99. The refined parameters of calcined samples of BF-x PT for 0.20≤x≤0.40 are given in table 3.3.

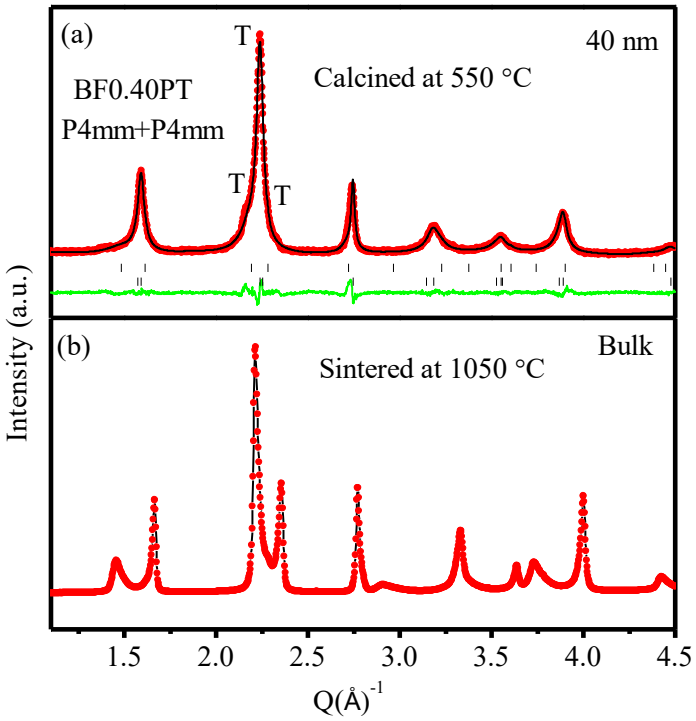

Fig.3.12 (a) Rietveld refinement profile of calcined BF-0.40PT powder (b) synchrotron x-ray powder diffraction pattern of bulk BF-0.40PT.

Table 3.3 Rietveld refinement results of Lab X-ray diffraction data of BF-0.xPT(x=0.20, 0.25, 0.30, 0.35 and 0.40)

BF0.xPT(x=0.20,0.25,0.30,0.35,0.40) calcined at 550℃		Fractional coordinates				Thermal Parameters ($Å^2$)	Lattice Parameters (Å)	Statistical parameters
		Atom	x	y	z			
BF0.20PT-550	Monoclinic phase	Bi/Pb	0.0	0.25	0.0	B_{iso}= 1.74(4)	a= 9.786(2) b= 5.5679(6) c= 5.6143(9) β= 125.5(5)	R_p= 13.9 R_{wp}= 18.3 R_{exp}= 14.0 χ^2 = 1.71
		Fe/Ti	0.226(9)	0.246(1)	0.684(1)	B_{iso}= 0.83(4)		
		O_1	-0.13(4)	0.123(3)	0.489(1)	B_{iso} =0.97(6)		
		O_2	0.303(6)	0.53 (2)	0.015(7)	B_{iso}= 0.44(3)		
		O3	0.274(5)	-0.03(3)	-0.04(2)	B_{iso}=0.63(4)		
	Tetragonal phase	Bi/Pb	0.0	0.0	0.0	B_{iso}= 1.06(1)	a=b=3.7890(5) c= 4.568(1)	
		Fe/Ti	0.5	0.5	0.534(9)	B_{iso}= 1.21(7)		
		O_1	0.5	0.5	0.274(5)	B_{iso}= 0.62(1)		
		O_2	0.0	0.5	0.676(8)	B_{iso}= 0.55(2)		
BF-0.25PT-550	Monoclinic phase	Bi/Pb	0.0	0.25	0.0	B_{iso}= 1.42(3)	a= 9.7922(3) b= 5.5706(1) c= 5.6131(1) β= 125.4(1)	R_p= 14.8 R_{wp}= 19.5 R_{exp}= 15.3 χ^2 = 1.62
		Fe/Ti	0.235(1)	0.25(8)	0.706(8)	B_{iso}= 1.57(8)		
		O_1	-0.11(2)	0.134(3)	0.493(2)	B_{iso} =0.97(6)		
		O_2	0.312(5)	0.56(1)	0.027(2)	B_{iso}= 0.44(3)		
		O3	0.262(3)	-0.01(6)	-0.04(5)	B_{iso}=0.63(5)		
	Tetragonal phase	Bi/Pb	0.0	0.0	0.0	B_{iso}= 1.14(1)	a=b=3.7967(1) c=4.5563(1)	
		Fe/Ti	0.5	0.5	0.523(2)	B_{iso}=1.18 (0)		
		O_1	0.5	0.5	0.212(2)	B_{iso}= 0.62(1)		
		O_2	0.0	0.5	0.647(1)	B_{iso}= 0.55 (1)		
BF-0.30PT-550	Monoclinic phase	Bi/Pb	0.0	0.25	0.0	B_{iso}= 1.39(1)	a= 9.7809(4) b= 5.5603(1) c= 5.588(7) β= 125.2(1)	R_p= 15.3 R_{wp}= 19.8 R_{exp}= 15.5 χ^2 = 1.63
		Fe/Ti	0.239(8)	0.252(5)	0.696(4)	B_{iso}= 0.94(8)		
		O_1	-0.07(1)	0.105(3)	0.46(6)	B_{iso} = 1.22 (1)		
		O_2	0.330(2)	0.550(3)	0.050(4)	B_{iso}= 0.81(2)		
		O3	0.278(9)	-0.02(1)	0.063(6)	B_{iso}= 0.78(9)		
	Tetragonal phase	Bi/Pb	0.0	0.0	0.0	B_{iso}= 1.24(4)	a=b=3.7766 (8) c=4.5668 (1)	
		Fe/Ti	0.5	0.5	0.474(3)	B_{iso}=0.25(2)		
		O_1	0.5	0.5	0.36(2)	B_{iso}=0.49(8)		
		O_2	0.0	0.5	0.696(3)	B_{iso}=0.54(1)		
BF-0.35PT-550	Tetragonal phase1	Bi/Pb	0.0	0.0	0.0	B_{iso}=1.09(5)	a=b=3.903(7) c=4.4235(2)	R_p=15.6 R_{wp}=19.1 R_{exp}=13.8 χ^2 = 1.50
		Fe/Ti	0.5	0.5	0.509(4)	B_{iso}=1.13(9)		
		O_1	0.5	0.5	0.265(3)	B_{iso}=0.84(6)		
		O_2	0.0	0.5	0.685(1)	B_{iso} = 0.44(3)		
	Tetragonal phase2	Bi/Pb	0.0	0.0	0.0	B_{iso}=1.12(6)	a=b=3.9181(5) c=4.0812(4)	
		Fe/Ti	0.5	0.5	0.487(9)	B_{iso}= 0.21(7)		
		O_1	0.5	0.5	0.302(2)	B_{iso}= 0.040(7)		
		O_2	0.0	0.5	0.680(1)	B_{iso}=0.78(8)		
BF-0.40PT-550	Tetragonal phase1	Bi/Pb	0.0	0.0	0.0	B_{iso}=1.3 (2)	a=b=3.8965(2) c=4.2404(9)	R_p=10.3 R_{wp}=11.6 R_{exp}=8.19 χ^2 = 1.99
		Fe/Ti	0.5	0.5	0.511(3)	B_{iso}=1.21(2)		
		O_1	0.5	0.5	0.260(2)	B_{iso}=0.94(5)		
		O_2	0.0	0.5	0.681(5)	B_{iso} = 0.45(3)		
	Tetragonal phase2	Bi/Pb	0.0	0.0	0.0	B_{iso}=1.2(5)	a=b=3.9415(6), c=4.03135 (2)	
		Fe/Ti	0.5	0.5	0.485(6)	B_{iso}= 0.28(5)		
		O_1	0.5	0.5	0.298(2)	B_{iso}= 0.041(4)		
		O_2	0.0	0.5	0.678(2)	B_{iso}=0.71(5)		

3.5.3.1Effect on the Unit Cell Parameters

Fig. 3.13 shows the composition dependence of the cell parameters of the tetragonal and monoclinic phases for the calcined powder. For better understanding of the cell parameters of the two phases, we have plotted equivalent perovskite cell parameters a_P, b_P, c_P of the monoclinic phase, which are related to the monoclinic cell parameters a_m, b_m, c_m as $a_P \approx a_m/\sqrt{6}$, $b_P \approx b_m/\sqrt{2}$, $c_P \approx c_m/\sqrt{2}$.

It is clear from the fig. 3.13, that lattice parameters are changes with change in compositions. The two tetragonal phase with different lattice constant are persist up to x=0.35. On further decreasing the concentration of $PbTiO_3$ in the solid solution of BF-xPT, a new monoclinic phase developed with a tetragonal phase and these two phases are persist up to x=0.2.

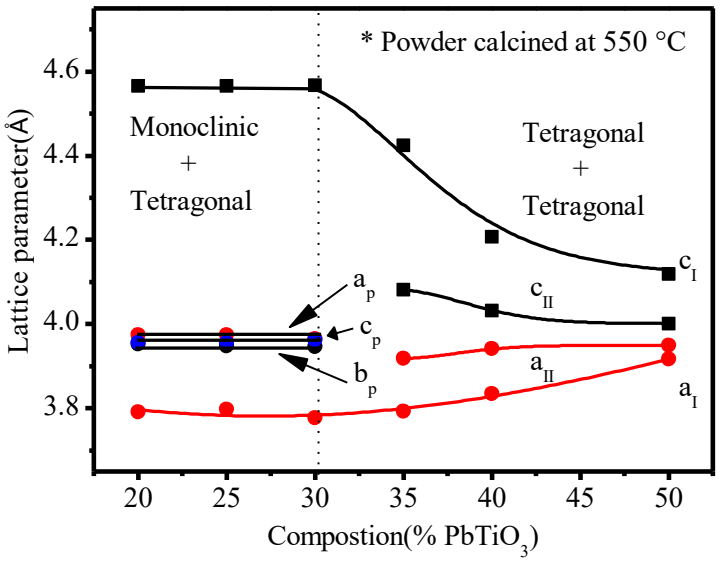

Fig.3.13 Variation of lattice parameters with composition for calcined powder of BF-x PT (x= 0.2 to 0.5) solid solution.

3.5.3.2 Effect of Size on the Phase Fraction and Tetragonality

Fig.3.14 shows the variation of the phase fraction of tetragonal phase with composition in crushed sample. In section 3.51, we have already discussed that sample calcined at 550℃ of size ~ 18 nm have two tetragonal phase, one with high teteragonality and another with low tetragonality at room temperature. We have plotted phase fraction of tetragonal phase present in composition range x=0.20 to 0.50. It shows that tetragonal phase continuously decreases towards $BiFeO_3$ rich side. It is also evident from this figure, the width of MPB region over which the tetragonal and monoclinic phase coexist in the BF-xPT solid solution is increased. [Bhattacharjee et al.(2007)] have shown that the width of MPB of bulk sample is lie in between of composition range $0.28 \leq x \leq 0.30$. But in our case on reduction of size, the MPB region extent to x=0.2 in $BiFeO_3$ rich end. It is important to note that MPB region gets extended only on the monoclinic side of the MPB and not on the tetragonal side. The result showing in fig. 3.14, reveals that width of the MPB region can be extended to the $BiFeO_3$ richer end as result of the size reduction.

The variation of tetragonality defined as $\eta = (c/a-1)$, with composition for the calcined powders is shown in Fig. 3.15 .The highest value of tetragonality observed so far for the calcined sample is 0.209(2) for x=0.30, which is much higher than as reported by Sai Sunder et. al (1995) and Woodward et. al (2003). The value of high tetragonality is due to strong covalent character of one of the Ti/Fe-O bonds in the [001] direction in tetragonal phase.

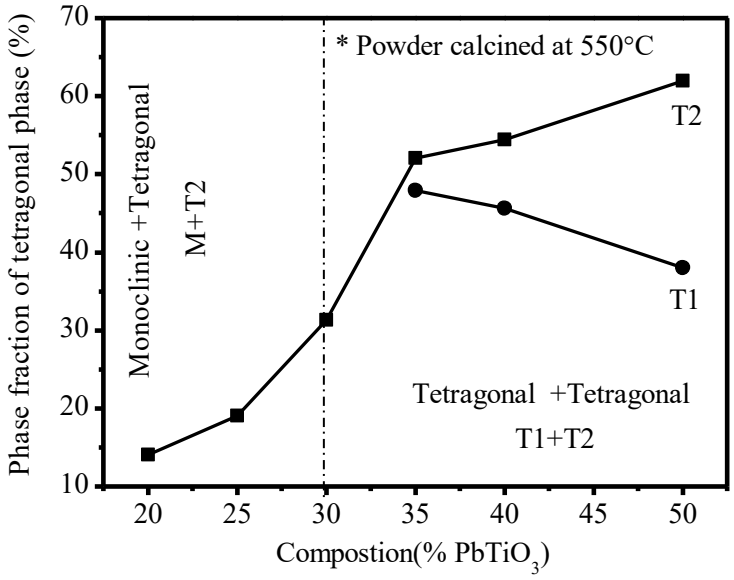

Fig.3.14 Variation of phase fraction of tetragonal phase with composition for calcined powder of BF-x PT (x= 0.2 to 0.5) solid solution.

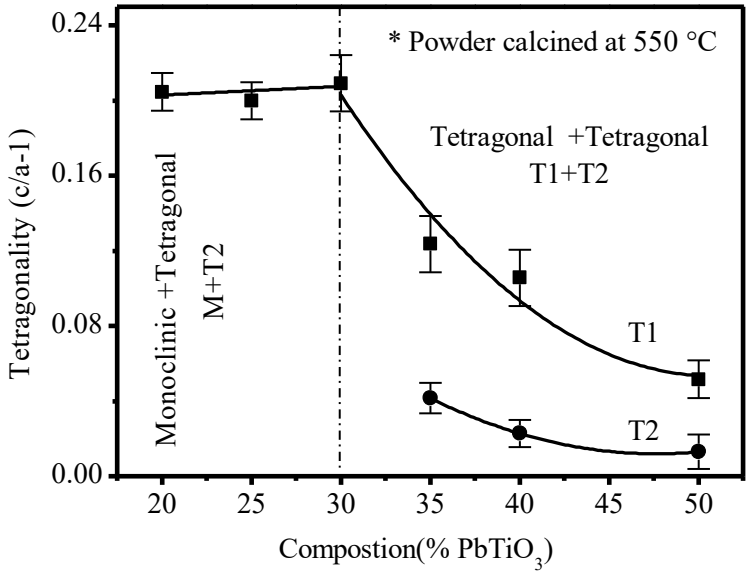

Fig.3.15 Variation of tetragonality (c/a-1) with composition calcined at 550℃

3.6 Summary and conclusions

The main conclusions of this chapter may summarize as under:

(1) The 120 nm powder of BF-0.5PT possesses a single tetragonal phase (space group P4mm) whereas the smaller size powders show coexistence of two tetragonal phases, a dominant tetragonal phase with higher tetragonality and a minority phase with relatively lower tetragonality, both in the P4mm space group, as confirmed by Rietveld refinement using Synchrotron x-ray powder diffraction data.

(2) Rietveld analysis using high resolution synchrotron x-ray powder diffraction data confirms that the space group of BF-0.25PT solid solutions is monoclinic Cc and not rhombohedral R3c for both bulk and nanocrystalline powders. This settles a longstanding controversy about the structure of these solid solutions towards $BiFeO_3$ rich end of the morphotropic phase boundary in $BiFeO_3$ -$xPbTiO_3$system.

(3) The crystal structure of BF -xPT($0.2 \leq x \leq 0.30$), calcined at 550℃ is shows the combination of monoclinic (Cc) and tetragonal (P4mm) phase within MPB region and two tetragonal phases with different tetragonality is present above the MPB i.e. ($0.35 \leq x \leq 0.50$)

(4) The refinements reveals that BF-xPT for x=0.30 exhibits highest tetragonality η=0.209(2), which is much higher than as reported by earlier.

The effect of size on the magnetic properties of BF-0.50PT has been taken up in the next chapter.

4.1 Introduction

In the previous chapter, we tried to settle the room temperature crystal structure of nano powder of BF-0.50PT using high energy synchrotron x-ray powder diffraction data.The nano-structured magnetic materials differ significantly from their bulk counterparts and have been exploited for several technological applications. The nanostructured ferromagnetic (FM) and ferrimagnetic (FerM) materials are commonly used in permanent magnets, magnetic data storage, logic devices, ferrofluids, biomedical devices etc. [Dormann et al. (1997),(1992), Fiorani (2005), Pankhurst et al. (2003)]. In recent years, nanostructured antiferromagnetic (AFM) materials have also received considerable attention for applications like spin valves, magnetic random access memory and AFM and FM composite based hard magnets [Mørup et al. (2007)].The tetragonal phase of BF-xPT has got several unusual characteristics : (1) it shows anomalously huge tetragonality (η= (c/a -1)) that is more than three times that of the commercial MPB ceramics like PZT, (2) tetragonality increases on approaching the MPB and becomes ~ 18.73% for x=0.31 whereas it decreases on approaching the MPB in PZT,(3) the high tetragonality phase does not result from the paraelectric (PE) cubic phase directly but by an isostructural phase transition from a low η phase, which gets formed first from the cubic paraelectric phase, below the curie temperature (4) and it shows very low T_N **(** ~ 209K for x=0.31**)** as compared to neighbouring monoclinic compositions with T_N ~ 473 K for x=0.27. Finite size effects in AFMs nanoparticles, nanorods and thin films have been investigated extensively [Molina-Ruiz et al. (2011), Kodma et al. (1996), Ambrose et al.(1996), Tang et al. (2003), Weschke et al. (2004)] and it has been shown that T_N decreases with decreasing particle size or the thin film thickness as per the predictions of Néel[Selbach et al. (2007)]. The decrease in T_N is found to be consistent with Binder's scaling theory of

critical phenomena in reduced dimension systems which give the following universal power law dependence of transition temperature [Binder (1972)].

$$\frac{T_N^b - T_N^{grain}}{T_N^b} = \left(\frac{d}{\xi_0}\right)^{-(1/\nu)} \quad \text{.....(4.1)}$$

where T_N^b and T_N^{grain} are the bulk and finite size AFM transition temperatures, d is the grain diameter, ξ_0 is the magnetic correlation length at 0 K and ν the critical exponent related to ξ.

4.2 Experimental

The different sizes of BF-0.5PT samples were synthesized by the methods discussed in chapter II. High energy synchrotron x-ray powder diffraction data were analysed by Rietveld method using the FULLPROF software package [Carvajal (1993)], discussed in chapter III. Magnetic characterization was carried out using a Quantum Design® Evercool II PPMS®. Magnetization vs temperature measurements were performed in the temperature range of 2.5K-390K in an applied field of 5000 Oe or 500 Oe on case to case basis, whereas magnetization vs applied field measurements were performed at selected temperatures up to a maximum field of 7 Tesla. Neutron powder diffraction measurements were carried out on high-resolution powder diffractometer SPODI at FRM-II, Garching, Germany. The incident neutron wavelength was 2.5367 Å. Approximately 10 g of the sample, contained in a cylindrical niobium holder with 50 μm wall thickness, 40 mm height, and 10 mm diameter, was used for these measurements. The data were collected at steps of 0.05° in the 2θ range from 1 to 157°. A closed cycle cryostat was used for sample temperature variation in the temperature range of 4 K to 500 K

4.3 Rietveld analysis of the neutron powder diffraction pattern

Neutron powder diffraction data were analyzed by Rietveld refinement technique using FULLPROF software package [Carvajal (2010)]. The magnetic structure is based on the propagation vector and the chemical unit cell which reveals the relation between moment orientations in the magnetic sub lattice. Representation theory is used to find out the possible magnetic structures and these structures are decomposed into irreducible representations (IR) of the little group G_k, which leave the propagation vector, k, invariant. G_k is a subgroup of the chemical space group G_0.The moment of a particular magnetic ion, say jth, can be written as a Fourier expansion

$$m_j = \sum_k \psi_j^k \exp\{-2\pi i k.r_j\} \quad \text{.....(4.2)}$$

where vector r_j represent the position of the jth magnetic ion. The general basis vector ψ_j^k is made up from contributions from several basis vectors, the ψ_ns , corresponding to a particular IR of G_k and can be written as,

$$\psi_j^k = \Sigma\, c_n \psi_n \quad \text{.....(4.3)}$$

where c_ns are the mixing coefficients.

For tetragonal magnetic structure representation of the Fe sublattice (1b site) at k= ½, ½, ½ can be expressed in terms of two IRs

$$\Gamma^{1b} = \Gamma_3 + \Gamma_5 \quad \text{.....(4.4)}$$

Where Γ_5 is two dimensional and Γ_3 is one dimensional. Refinement with the two models (Γ_3 and Γ_5) shows that the second IR (Γ_5) gives better fit [Bhattacharjee et al (2010)]. Basis vector of Γ_1 gives a G-type of antiferromagnetic structure with the magnetic moments along the crystallographic c axis. There are two basis vector for Γ_5 and the

combined structure with these two basis vectors are again of G-type but with the magnetic moment in the ab plane. The character table and the basis vectors of these two IRs of the tetragonal phase are given in Table 4.1

Table 4.1 Character table and basis vector (magnetic) of space group P4mm at k = (1/2, 1/2, 1/2)

Irreducable Representation	Symmetry elements (Kovalev)							
	{1|000}	{2_00z|000}	{4+_00z|000}	{4-_00z|000}	{m_x0z|000}	{m_0yz|000}	{m_x-z|000}	{m_xxz|000}
Γ_1	1	1	1	1	1	1	1	1
Γ_2	1	1	1	1	-1	-1	-1	-1
Γ_3	1	1	-1	-1	1	1	-1	-1
Γ_4	1	1	-1	-1	-1	-1	1	1
Γ_5	1 0 0 1	-1 0 0 -1	i 0 0 -i	-i 0 0 i	0 1 1 0	0 -1 1 0	0 –i i 0	0 i -i 0

Irreducable Representation	**Basis vector**	**1b site**	
		(1/2,1/2,z)	
Γ_3	$\tau_{1,1}$	Re Im	(0 0 1)
Γ_5	$\tau_{5,1}$	Re Im	(0 0 1) (0 0 1)
	$\tau_{5,2}$	Re Im	(0 0 1) (0 0 1)

4.4 Result and diacussion

4.4.1 Magnetization studies of BF-0.5PT powder

BF-0.5PT with average particle sizes of ~ 18, 31, 45 and 120 nm are selected for the magnetic studies. [Details are given in Chapter II and III].Temperature (T) dependence of magnetization (M) of BF-0.50PT was investigated at a magnetic field of 5000 Oe during heating in the temperature range of 2K to 390 K for 120 nm, 45 nm, 31 nm and 18 nm size powders in zero-field cooled (ZFC) and field cooled (FC) modes . The results are shown in fig.4.1 (a to d). In M(T) of curves BF-0.5PT, the magnetization starts increasing below a certain temperature with decreasing temperature like in ferromagnetic, ferrimagentic [Cullity (1972)] or canted antiferromagnetic system. Therefore, the behaviour of M(T) curve of BF-0.5PT is probably due to canted antiferromagnetic ordering in which the weak ferromagnetic component appears below the magnetic transition temperature. The ZFC M-T plot of the 120 nm size particles shows a Néel transition temperature T_N ~ 120K (see the inset also) similar to that reported in bulk powders of BF-0.5PT [Binder (1972)]. Intriguingly, on reducing the particle size to 45 nm, 31 and 18 nm, the Néel temperature increases drastically to 230, 250 and 350K, respectively, as can be seen from various insets to Fig 4.1. The anomaly at T_f ~17K in the ZFC M-T plot of the bulk is known to be due to spin glass freezing [Zhu et al. (2008)].

$BiFeO_3$ shows linear M-H curve because of the presence of the spatially incommensurate modulated spiral spins structure of approximate wavelength of 62 nm [Lebeugle et al. (2007)]. In this scenario, one expects weak ferromagnetism due to spin canting in the shell region of the 18 nm size nanoparticles of BF-0.5PT as observed in similar core-shell type systems in non multiferroic AFM oxides [Benitez et al. (2008).

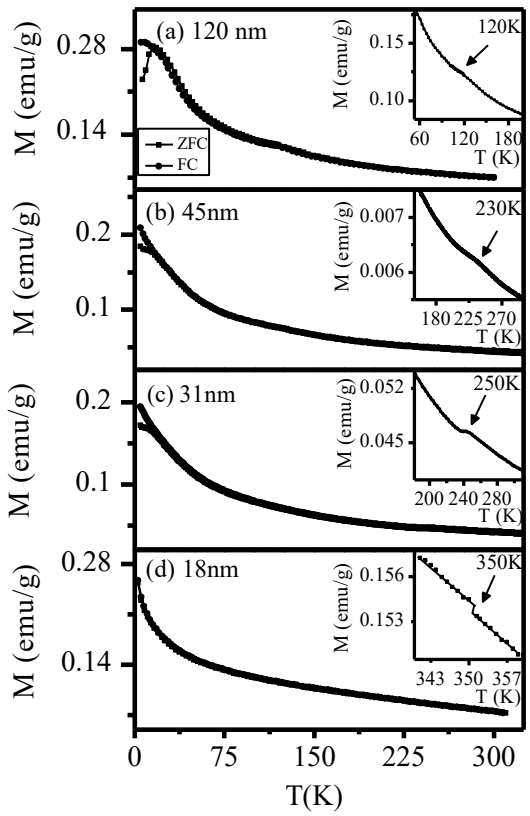

Fig.4.1 The temperature dependence of the FC and ZFC magnetizations of BF-0.5PT: (a–d) 120, 45, 31 and 18 nm size powders under magnetic field of 5000 Oe, The insets of (a to d) depict magnified plot near T_N

This was confirmed by the M-H measurements, the results of which are shown in Fig 4.2. It is evident from Fig 4.2(a) that the M-H plots for 120 nm, 45 nm and 31 nm size powders are straight lines confirming their paramagnetic nature at room temperature, whereas the 18 nm size particles exhibit nonlinear M-H curve, with a little loop opening. With decreasing temperature, the M-H loop of 18 nm size particles opens up further as can be seen from the two insets of Fig 4.2(b) which compare the M-H plots for 18 nm size particles at 300 K and 5 K. Further, the M-H loop in Fig 4.2(b) inset reveals an exchange bias (E_B) of ~ 337 Oe at 5K, which decreases with increasing temperature for the same particle size. The E_B decreases with increasing particle size also for the same

temperature. For example, the E_B at 5 K is ~17 Oe and ~8 Oe for 31 nm and 45 nm size powders, respectively, while it is absent for the bulk powder (see Fig 4.2(c) inset).

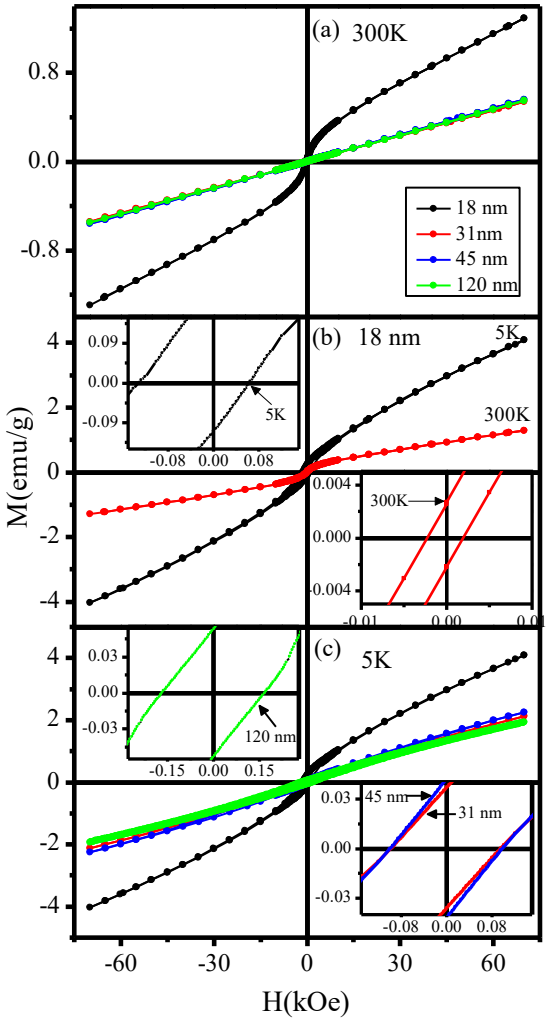

Fig.4.2 M-H plots for (a)18, 31, 45,120 nm size powders at 300K, (b) 18 nm particles at 300 and 5K and (c) 18, 31, 45, 120 nm size powders at 5K. Insets of (b) and (c) compare exchange bias at 5K and 300K for 18 nm, and at 5K for 120 and 31 nm powders.

The more pronounced E_B, as shown in the inset of Fig 4.2(b), in the smallest size particles (~18 nm) is due to higher surface to volume ratio of 18 nm particles leading to more number of spins in the surface layers constituting the shell region.

To verify the exchange bias which is present in nano sample, we again capture the M-H measurement using the Quantum Design Evercool MPMS3 to a very close step size of 20Oe at room temperature. As shown in fig. 4.3 hysteresis loops were measured in both the zero-field-cooling (ZFC) and field-cooling (FC) condition. After being cooled in a magnetic field of $\pm 5T$ we observe that, there is a corresponding shift in the hysteresis loop in both horizontal and vertical FC hysteresis curve.

Upon cooling the sample in positive magnetic field results in a negative shift of the hysteresis loop and vice versa. A exchange bias with a value of ~328 Oe is detected from the shift along the field axis of the FC curve which is approximately same as found by earlier result. The interface between the FM component of the canted spins in the shell region and the collinear AFM spins in the core (of BF-0.50PT) is responsible for the exchange bias effect as observed in other systems also [Benitez et al. (2008), Yusuf et al. (2013), Manna et al. (2014). Thus our M-H plot showing E_B effect not only confirms the coexistence of AFM and weak FM ordering but also reveals that they arise from a core-shell type of nanostructure of individual nanoparticles.

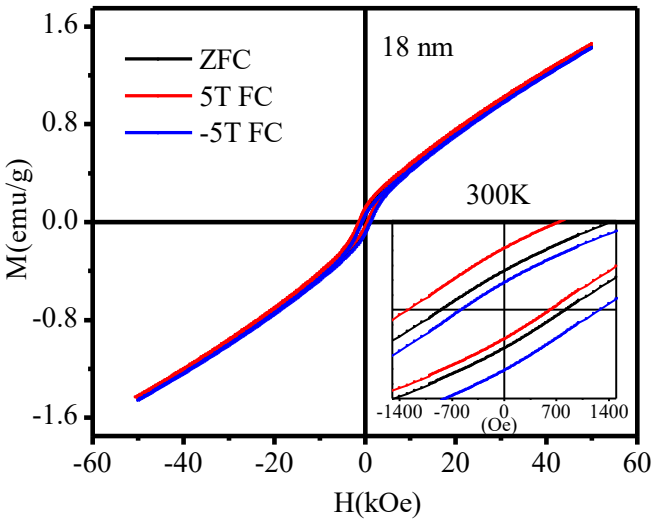

Fig.4.3 The field-dependent magnetization hysteresis (M-H) loops of BF-0.5PT of size 18nm. Inset shows the shifting of curve with fields.

4.4.2 Neutron diffraction studies

In order to realize the arrangement of magnetic moments in iron sublattice below T_N, powder neutron diffraction studies have been carried out in temperature range from 4K to 300K for nano and 4K to 460K for bulk powder. The temperature evolution of the magnetic peak corresponding to propagation vector k=½ ½ ½ in the neutron powder diffraction patterns is shown in Figs 4.4 (a) and 4.4(b) for bulk and 18nm size powders, respectively in the 2θ range from 30 to 38 degrees. The magnetic peak occurring just before the psuedocubic (100) nuclear peak is due to the antiferromagnetic ordering of the spin. The intensity of peak decreases with increasing temperature but does not become zero at T_N. In the bulk samples, the AFM peak (marked with asterisk in the figure) appears below T_N ~120K whereas it is present even at room temperature in 18nm size powder.

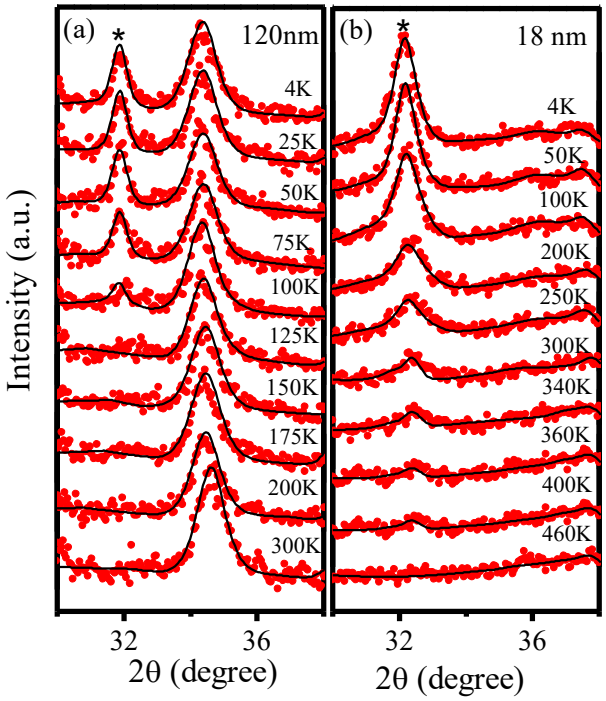

Fig. 4.4 Temperature dependent powder neutron diffraction profile of bulk and nano BF-0.5PT samples. Corresponding temperatures are shown in figures.

This clearly shows a drastic enhancement of T_N in 18nm size powder. The variation of the integrated intensity of the ½ ½ ½ magnetic peak with temperature shown in Fig 4.5 (a) reveals T_N ~120K in agreement with the T_N determined from ZFC M-T measurements (Fig. 4.1). The magnetic neutron peaks of 18 nm particles have sharp and diffuse (broad) components (see Fig 4.5(b) which depicts two deconvoluted Lorentzians) linked with the coexisting high and low tetragonality phases, respectively, as confirmed by Rietveld refinements using SXRPD data (see chapter III). The diffuse component of the magnetic scattering is dominant above 250K. The variation of the integrated intensity of the sharp component with temperature for 18nm size powder shows a linear behaviour upto ~250K and its extrapolation to zero intensity gives a T_N of ~350 K in agreement with the M(T) results. Thus there is a drastic enhancement of T_N with respect to T_N =120K of the bulk

powder. The diffuse component shows temperature dependence different from that of the sharp component and the corresponding T_N is still higher, as small residual intensity can be seen at the AFM peak position even in 360 and 400 K profile in Fig. 4.5 (b). We propose that the diffuse component of the magnetic peak with shorter correlation length is due to spin disorder in a thin shell region of the surface layers of the nanoparticles. In this scenario, one expects weak ferromagnetism due to spin canting in the shell region of the 18 nm size nanoparticles of BF-0.5PT as observed in similar core-shell type systems in non multiferroic AFM oxides [Benitez et al. (2008)]. This weak ferromagnetism should be present even at room temperature as the corresponding T_N is well above the room temperature for 18 nm size particles.

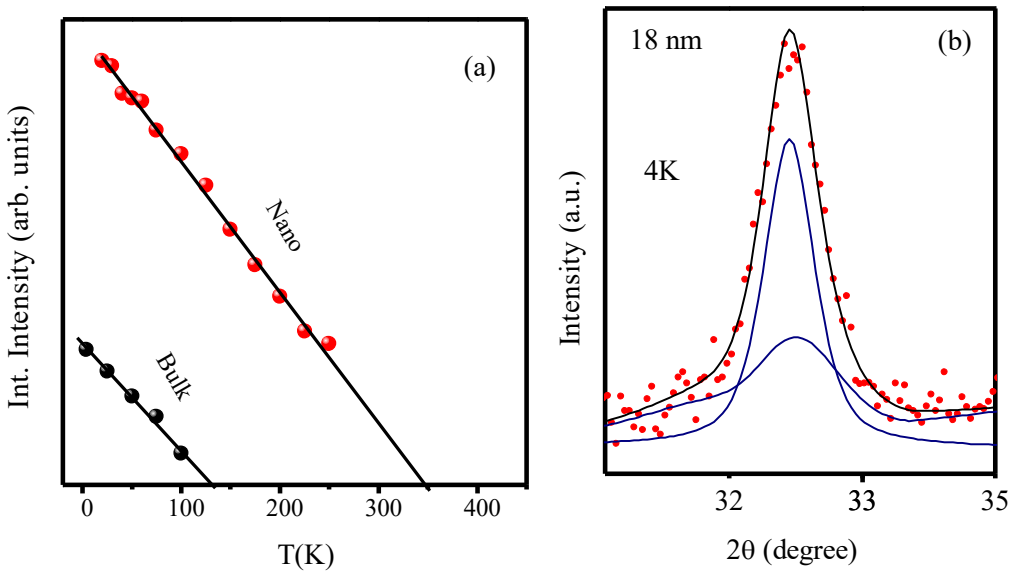

Fig. 4.5 (a) Variation in the integrated intensity of the magnetic peak with temperature for bulk and nano size powders. Dots represent measured data points, while the continuous line corresponds to the least-squares fitted Lorentzian(s). (b) Deconvolution of the magnetic peak of 18 nm size powder showing two different magnetic correlation lengths (ξ).

4.4.3 Role of super exchange interaction

The enhancement of T_N with size reduction is unique to MFAFMs. It is a consequence of the subtle interplay between the ferroelectric distortion and the strength of the superexchange interaction in the multiferroic BF-0.5PT. Table 4.2 lists the lengths of Fe^{3+}- O^{2-} bond lengths in the [001] direction for the bulk and the 18 nm size powder, as calculated using the positional coordinates obtained by Rietveld refinement of SXRPD patterns [see chapter III]. The longer Fe^{3+}- O^{2-} bond length (labelled as Fe-O_{1b} in Table 4.2) in the bulk powder is too big (2.571 Å) as compared to the sum of the ionic radii of Fe^{3+} and O^{2-} (~2.045 Å) to have any orbital overlap required for superexchange interactions in [001] direction in the bulk powders. As a result, the AFM superexchange interaction pathways are confined to [100] and [010] directions only.

Table 4.2 Fe-O bond lengths (Å of the dominant phase constituting the core of BF-0.5PT samples as a function of particle size

Size (nm)	Bond length (Å)		
	Fe-O_{1a}	Fe-O_{1b}	Fe-O_2
18	1.787	2.348	2.013
31	1.790	2.369	1.970
45	1.792	2.460	1.973
120	1.822	2.571	1.968

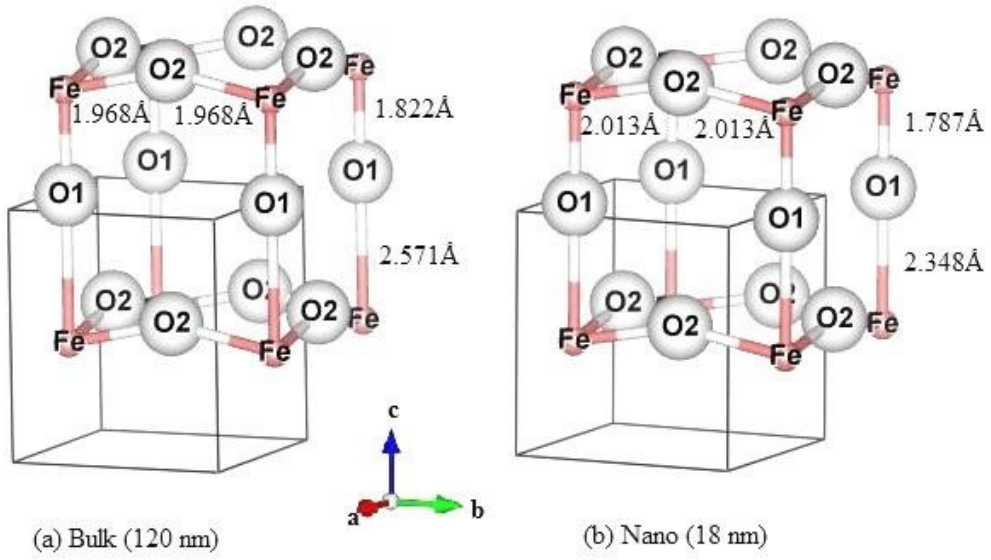

Fig.4.6 Fe-O-Fe exchange pathways (a) Bulk (b) 18 nm of $BiFeO_3$-0.50$PbTiO_3$

As the longer Fe^{3+}- O^{2-} bond in the [001] direction decreases systematically with particle size reduction (see Table 4.2 for bond length of the 18 nm size powder), there is a gradual enhancement of superexchange interaction in the [001] direction also. This crossover from essentially 2d AFM interactions in the bulk powders to 3d AFM interactions in nanoparticles of BF-0.50PT is responsible for the drastic rise in the T_N as a result of size reduction. Fig.4.6 shows the superexchange percolating path of Fe-O-Fe for bulk and nano sample of BF-0.5PT, for the better understanding of this system.

Thus, the physics of size effect in multiferroic AFM systems is entirely different from that in conventional AFM systems.

4.4.4 Evidence of enhancement of T_N at atomic level:

Although the XRD study shows that presence of two tetragonal phases in nano BF-0.5PT samples at room temperature. Temperature dependent neutron diffraction study was carried out for 18 nm size samples not only answer to structural information but also precisely determine the oxygen coordinates which is not possible through XRD data. It is

already well established refinement for bulk sample of BF-0.31PT [Bhattacharjee et al.(2010)], so our focus to visualized it nano part of this composition.

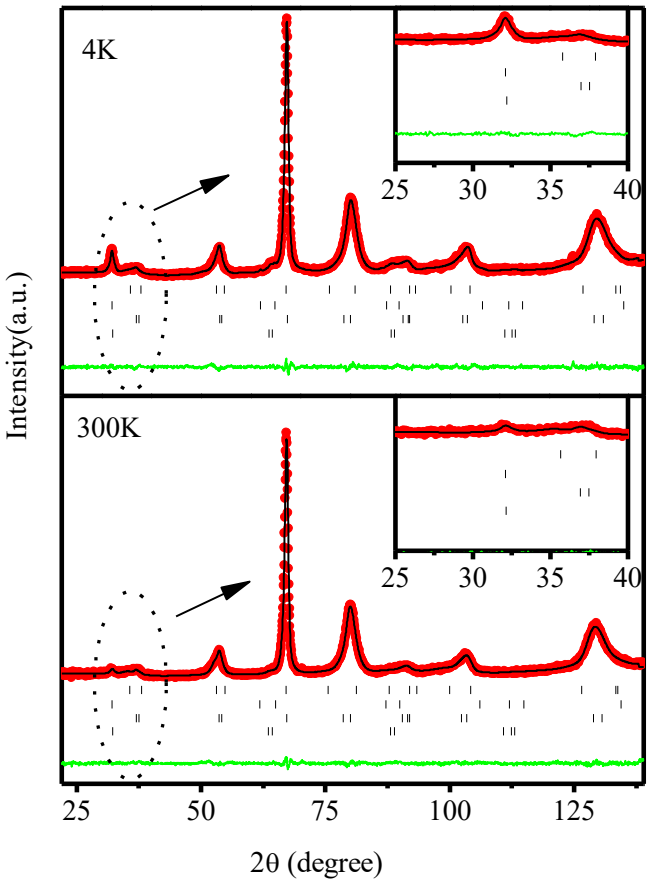

Fig. 4.7 Observed (dotted), calculated (continuous line) and difference profiles (bottom line) obtained from Rietveld refinement of BF-0. 5PT using P4mm space group. The inset shows the magnetic peak of nano powder at temperature of 4K and 300K.

We carried out Rietveld refinements for the BF-0.5PT sample having lowest particle size (~18 nm). Fig.4.7 shows neutron pattern at temperature of 4K and 300K. The parameter obtained from refinement is listed in table 4.3

Table 4.3 Rietveld refined positional coordinates, thermal parameters and lattice parameters of 18 nm size powder of BF-0.50PT at 4K and 300K. The magnetic R-factor for the coexisting phase is rather high due to the diffuse nature of the neutron peak component.

BF0.5PT with size 18 nm		Fractional coordinates				Thermal Parameters ($Å^2$)	Lattice Parameters (Å)	Statistical parameters
		Atom	x	y	z			
4K	Tetragonal phase-1	Bi/Pb	0.0	0.0	0.0	$B_{11}=B_{22}$= 0.146(4), B_{33}=0.183(9)	a=b= 3.9075(4) c= 4.129(1)	R_p= 10.0 R_{wp}= 9.49 R_{exp}= 7.37 χ^2 = 1.659 Magnetic R-factor: 1.27
		Fe/Ti	0.5	0.5	0.509(3)	B_{iso}=1.8(2)		
		O1	0.5	0.5	0.121(2)	$B_{11}=B_{22}$= 0.019(6) B_{33}= 0.05(1)		
		O2	0.0	0.5	0.649(1)	$B_{11}=B_{22}$= 0.091(5) B_{33}= 0.070(6)		
	Tetragonal phase-2	Bi/Pb	0.0	0.0	0.0	$B_{11}=B_{22}$= 0.028(2), B_{33}=0.005(3)	a=b= 3.9458(2) c= 4.0026(5)	
		Fe/Ti	0.5	0.5	0.599(2)	B_{iso}=1.6(1)		
		O1	0.5	0.5	0.056(2)	$B_{11}=B_{22}$= 0.052(2), B_{33}= 0.00006(1)		
		O2	0.0	0.5	0.576(1)	$B_{11}=B_{22}$= 0.005(3), B_{33}= 0.140(4)		
300K	Tetragonal phase-1	Bi/Pb	0.0	0.0	0.0	$B_{11}=B_{22}$= 234 (3), B_{33}= 0.073(9)	a=b= 3.9010 (5) c= 4.1442 (3)	R_p= 9.52 R_{wp}= 8.89 R_{exp}= 7.11 χ^2 = 1.56 Magnetic R-factor: 2.21
		Fe/Ti	0.5	0.5	0.512 (9)	B_{iso}= 1.848 (3)		
		O1	0.5	0.5	0.120 (1)	$B_{11}=B_{22}$ 0.045(6) B_{33}= 0.006 (1)		
		O2	0.0	0.5	0.651 (6)	$B_{11}=B_{22}$= 0.17 (2) B_{33}= 0.15 (2)		
	Tetragonal phase-2	Bi/Pb	0.0	0.0	0.0	$B_{11}=B_{22}$= 0.050(2), B_{33}= 0.005(7)	a=b= 3.9484 (3) c= 4.0079 (2)	
		Fe/Ti	0.5	0.5	0.605 (2)	B_{iso}=1.8(1)		
		O1	0.5	0.5	0.038 (2)	$B_{11}=B_{22}$= 0.041 (2), B_{33}= 0.0009 (1)		
		O2	0.0	0.5	0.555 (3)	$B_{11}=B_{22}$= 0.0002 (3), B_{33}= 0.15 (4)		

As far as the magnetic structure of BF-0.5PT is concerned, there is only one magnetically active cation, Fe^{3+}, in this solid solution and the magnetic structure therefore corresponds to the arrangement of magnetic moments of Fe^{3+} sublattice only. The unit cell volume shows a small but distinct change around 350 K (see Fig.4.8). The temperature ~350 K at which we observe anomalies in the tetragonal unit cell volume, coincides with the magnetic transition temperature T_N ~350 K obtained by the magnetization studies. These

anomalies in the unit cell parameters at T_N reveal the presence of magnetoelastic coupling in BF-0.50PT. There is another isostructural phase transition across T_N was observed which is obtained by Rietveld refinement of nano sample.

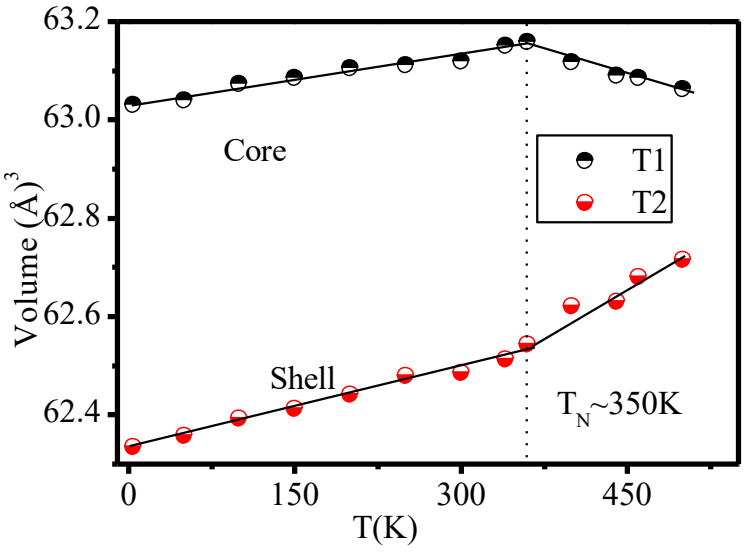

Fig. 4.8 Temperature dependent variation of unit cell volume obtained by powder neutron diffraction profile of 18nm BF-0.5PT samples.

Isostructural phase transition (IPT) are very rare [Ranjan et al (2005)] but have been reported across T_N in another multiferroics $LuMnO_3$ and $YMnO_3$ [Lee et al (2008)] recently but at very low temperatures. More recently, an isostructural phase transition has also been reported in the (1-x)$BiFeO_3$- x$PbTiO_3$ system at high temperatures close to ferroelectric phase transition rather than magnetic transition temperature [Bhattacharjee et al. (2011)].

The variation of the ordered magnetic moment per Fe^{3+} ion, obtained by Rietveld refinements, as a function of temperature in the range 2-340 K is shown in Fig.4.9. The ordered moment were fitted by power law $\mu(T) = \mu_0(1-T/T_N)^{\beta}$ using μ_0, T_N and β as fitting parameters for the data 2K<T<350 K. The fits are shown as solid lines through the data

points. The fits give β = 0.41(3) and T_N~ 350(5) from the ordered moment curve. The value of critical exponent β obtained from calculated ordered magnetic moment data is close to half which suggests that the antiferromagnetic phase transition may be second order in nature.

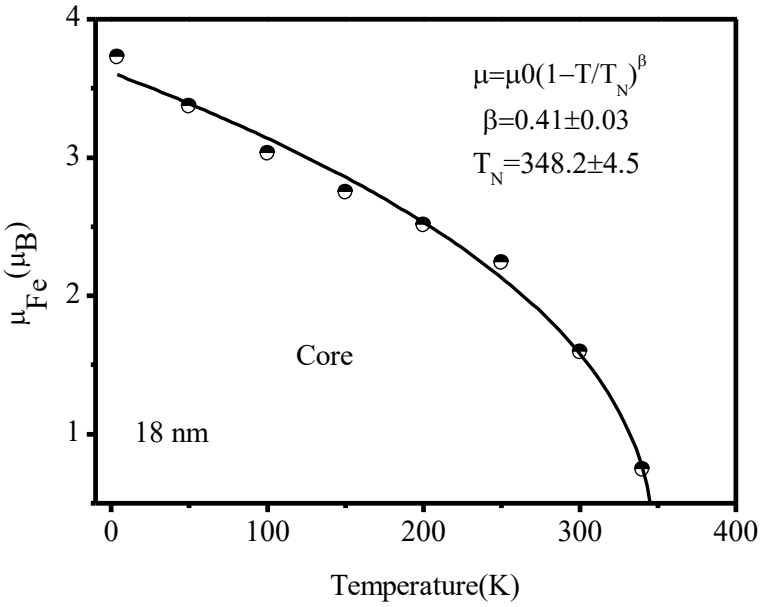

Fig. 4.9 Temperature dependence of ordered magnetic moment (half filled circle) obtained from the Rietveld refinement of neutron powder diffraction data fitted curve with $\mu(T) = \mu_0(1\text{-}T/T_N)^{\beta}$

4.5 Summary and conclusions

The main conclusions of this chapter may summarized as under:

(1) The Néel temperature (T_N) of BF-0.5PT where increases from ~120K in bulk powders to ~350K in 18nm size ferroelectric powders. It is possible to raise the Néel temperature (T_N) substantially (upto ~ 200K) through particle size reduction. This extraordinary enhancement of T_N is linked with the tunablity of the strength of the superexchange interaction through a decrease in the ferroelectric distortion in low dimensional systems due to finite size effects.

(2) The nano sample also shows a huge amount of exchange bias (E_B) of ~ 337 Oe at 5K, which confirms core-shell type structure.

(3) There is significant shift in the lattice parameter obtained from Rietveld refinement of the nuclear and magnetic structures using neutron powder diffraction data at magnetic transition temperature without affecting the symmetry.

The magnetic properties towards the $BiFeO_3$ end of MPB for bulk samples shows variety of exotic phenomenon like spin reorientation temperature, sudden increase in the Neel transition temperature after crossing the boundary. The size plays an important role in magnetic properties of BF-0.50PT samples. It will be interesting to explore the role of size for the composition towards $BiFeO_3$ side as well. Next chapter deals with the magnetic studies on BF-0.25PT sample and the effect of size on that.

5.1 Introduction

In previous chapter, we reported an anomalous increase in T_N from120 K to ~350K on reducing the size from 120 nm to 18 nm in the tetragonal phase of (1-x)$BiFeO_3$-x$PbTiO_3$solid solution for x=0.50.The tetragonal phase of BF-xPT is unusual because of its large tetragonality (η= (c/a -1) that affects the superexchange interactions also. For example, the T_N of the monoclinic phase of BF-xPT with x=0.27is ~473K which suddenly drops to ~ 210Kfor x=0.31 as a result of the morphotropic structural phase transition to the tetragonal phase in the bulk samples [Bhattacharjee et al. (2010)].This is quite intriguing. Had this drop been due to due to slight increase (4%) in disorder content of the magnetic sublattice, the T_N should have been ~ 453K, being the extrapolated value of T_N from the monoclinic side. It was argued that the low value of T_N of bulk tetragonal compositions across the MPB is due to the large ferroelectric distortion (η=c/a-1) caused by the off centering of Fe^{3+}/Ti^{4+} ions in the oxygen octahedral environment that breaks the covalent bond, and hence the superexchange interaction pathway, along the [001] direction reducing the dimensionality of the AFM state to d= 2 (ie, 2d-AFM) [Bhattacharjee et al. (2010), Yashima et al. (2011)]. More significantly, it was demonstrated that the anomalous increase in T_N on decreasing the particle size of the tetragonal compositions is linked with the crossover from nearly 2d AFM ordering in bulk to a 3d AFM ordering in smaller particles due to reestablishment of superexchange interactions in the [001] direction as a result of reduced ferroelectric distortion in the tetragonal structure[chapter IV].Thus the anomalous increase in T_N with decreasing size is a consequence of the complex interplay between ferroelectric distortion and the strength of the superexchange interactions both of which can be modulated through size.

As mentioned earlier, the structure of BF-xPT changes from tetragonal (space group P4mm) for x≥0.31 to monoclinic (space group Cc) for x ≤ 0.27 while the two phases coexist in the morphotropic phase boundary (MPB) region [Bhattacharjee et al (2007)].The nature of 3d AFM ordering in the pseudorhombohedral monoclinic phase of BF-xPT is similar to the 3d AFM phase of pure BF, except for the fact that PT substitution leads to the lowering of the space group symmetry from R3c to Cc[Bhattacharjee et al.(2010)].It is of interest to investigate the effect of particle size in such monoclinic compositions also to understand the role of ferroelectric distortion on the T_N. We show here that unlike pure BF, where T_N decreases with decreasing particle size as per the predictions of the scaling theories, the T_N of the monoclinic phase of BF-xPT in fact increases with decreasing particle size [Binder (1972)].Our findings highlight an ignored facet of magnetoelectric coupling in multiferroics in the literature where by ferroelectric distortion and its manipulation through particle size can be used to tailor the strength of the magnetic interactions and hence the magnetic transition temperatures. We present the results of high resolution synchrotron x-ray diffraction (SXRD), neutron powder diffraction (NPD) and magnetization measurements on both bulk and nanocrystalline powders of a pseudorhombohedral monoclinic composition of BF-xPT with x=0.25 to illustrate the anomalous size effect.

5.2 Experimental

Powders of BF-0.25PT solid solution with different sizes were synthesized using sol-gel technique the details of which are given in chapter II. X-ray diffraction (SXRD) patterns were also recorded at high resolution powder diffraction beamline P02.2 at PETRAIII, DESY, Hamburg, Germany for resolving the controversy about the true space group symmetry (R3c or Cc) of BF-0.25PT discussed in chapter III.

Magnetic measurements at and above room temperature were carried out using a Quantum Design Evercool MPMS3 with a high temperature attachment capable of going up to 1000 K. Temperature dependent magnetization M(T) measurements were carried out on zero field cooled samples while heating under a magnetic field of 500 Oe. Magnetization (M) vs applied field (H) hysteresis measurements were also performed at different temperatures up to a field of 5 Tesla.

Neutron powder diffraction (NPD) patterns were recorded on the high-resolution powder thermal neutron diffractometer HRPT at the Swiss Spallation Neutron Source (SINQ) at Paul Scherrer Institute, Switzerland. The neutron beam with a wavelength of 1.494 Å obtained by using a (533) refection from a vertically focusing Ge-monochromator was used. The diffraction signal was recorded using a position-sensitive detector in the 2θ range of 5 and 165^0.

Rietveld refinements were carried out using FULLPROF package [Carvajal (1993)]. For refining the magnetic structure, Rietveld refinements were carried out using the FULLPROF packageand BasIrreps software in the same package.

5.3 Rietveld analysis of the neutron powder diffraction pattern

As far as the magnetic structure of BF-0.25PT is concerned, there is only one magnetically active cation, $Fe^{3+,}$ in this solid solution, and the magnetic structure therefore corresponds to the arrangement of magnetic moments of Fe^{3+} sublattice only.

Since the Cc space group of BF-0.25PT already possesses a doubled perovskite cell, the magnetic structure can be represented by the propagation vector k = (0,0,0). The magnetic representation of the Fe sublattice (4a Wyckoff site) can be decomposed into two irreducible representations (IRs), each having three basis vectors, as, $\Gamma^{4a} = 3[\Gamma^{1} + \Gamma^{2}]$, leading to two possible configurations of the magnetic moments in the monoclinic phase:

$$\Gamma_1: G^X=S_1^X-S_2^X+S_3^X-S_4^X,\ F^Y=S_1^Y+S_2^Y+S_3^Y+S_4^Y,\ G^Z=S_1^Z-S_2^Z+S_3^Z-S_4^Z$$

$$\Gamma_2: F^X=S_1^X+S_2^X+S_3^X+S_4^X,\ G^Y=S_1^Y-S_2^Y+S_3^Y-S_4^Y,\ F^Z=S_1^Z+S_2^Z+S_3^Z+S_4^Z$$

where, the symbols F and G stand for ferromagnetic and G-type antiferromagnetic arrangements of moments (Bertaut's notation [Bertaut (1968)]) while Si (i=1 to 4) stand for the components of the ith atomic site. The superscripts X, Y, and Z in G, F and Si represent the [100], [010] and [001] directions of the monoclinic cell. The character table and the basis vectors of the two IRs are given in Table 5.1(a,b). It is evident that the magnetic structure due to both the IRs will be noncollinear resulting from the superposition of ferromagnetic and antiferromagnetic components of the net moments.

Table 5.1(a): Character table and basis vector (magnetic) of space group Cc at $\boldsymbol{k}$ = 0,0,0

Irreducible Representation	Symmetry elements (Kovalve)	
	{1|0,0,0}	{σ|0.5,0,0}
Γ_1	1	1
Γ_2	1	-1

Irreducible Representation	Basis Vector		4a site	
			(x,y,z)	(x, -y, z+1/2)
Γ_1	$\tau_{3,1}$	Re	(1 0 0)	(-1 0 0)
		Im		
	$\tau_{3,2}$	Re	(0 1 0)	(0 1 0)
		Im		
	$\tau_{3,3}$	Re	(0 0 1)	(0 0 -1)
		Im		
Γ_2	$\tau_{5,1}$	Re	(1 0 0)	(1 0 0)
		Im		
	$\tau_{5,2}$	Re	(0 10)	(0 -1 0)
		Im		
	$\tau_{5,3}$	Re	(0 0 1)	(0 0 1)
		Im		

Table 5.1(b): Character table and basis vector (magnetic) of space group Cc at $\boldsymbol{k}$ = 0,0,1

Irreducable Representation	Symmetry elements (Kovalve)	
	{1|0,0,0}	{σ|0.5,0,0}
Γ_1^{001}	1	1
Γ_2^{001}	1	-1

Irreducable Representation	Basis Vector		4a site	
			(x,y,z)	(x, -y, z+1/2)
Γ_1	$\tau_{3,1}$	Re	(1 0 0)	(-1 0 0)
		Im		
	$\tau_{3,2}$	Re	(0 1 0)	(0 1 0)
		Im		
	$\tau_{3,3}$	Re	(0 0 1)	(0 0 -1)
		Im		
Γ_2	$\tau_{5,1}$	Re	(1 0 0)	(1 0 0)
		Im		
	$\tau_{5,2}$	Re	(0 10)	(0 -1 0)
		Im		
	$\tau_{5,3}$	Re	(0 0 1)	(0 0 1)
		Im		

5.4 Results and discussion

5.4.1 Room temperature Rietveld refinement of BF-0.25PT

Synchrotron x-ray powder diffraction (SXRD) patterns of 200,220, 222 and 400 reflections of BF-0.25PT for the sizes of ~ 150, 300, 500 and 2000 nm are given in Chapter III.In order to remove any ambiguity due to limited number of peaks in the SXRD pattern, we also used high resolution and higher "*q*" neutron diffraction data collected well above the Néel transition temperature T_N where no magnetic peak is present, for structure refinement. The results of Rietveld refinement of the nuclear structure at high temperature (750K) using neutron diffraction pattern is shown in fig. 5.1 for Cc (core)+Cc (shell), Cc (core)+R3c (shell) and Cc (core) + P4mm (shell)and R3c

(core) + P4mm (shell) structural models. As in the case of SXRD data, we find that Rietveld refinement using neutron data also increases χ^2 for the two phase models with respect to that of the single phase refinement using Cc space group. This proves that the increase in χ^2 for two phase refinements is not due to limited number of peaks in SXRD patterns. This suggests that the system remains in the monoclinic Cc phase even after size reduction with insignificant contribution due to the disordered atoms, if any, in the shell region which cannot be captured by Rietveld technique.

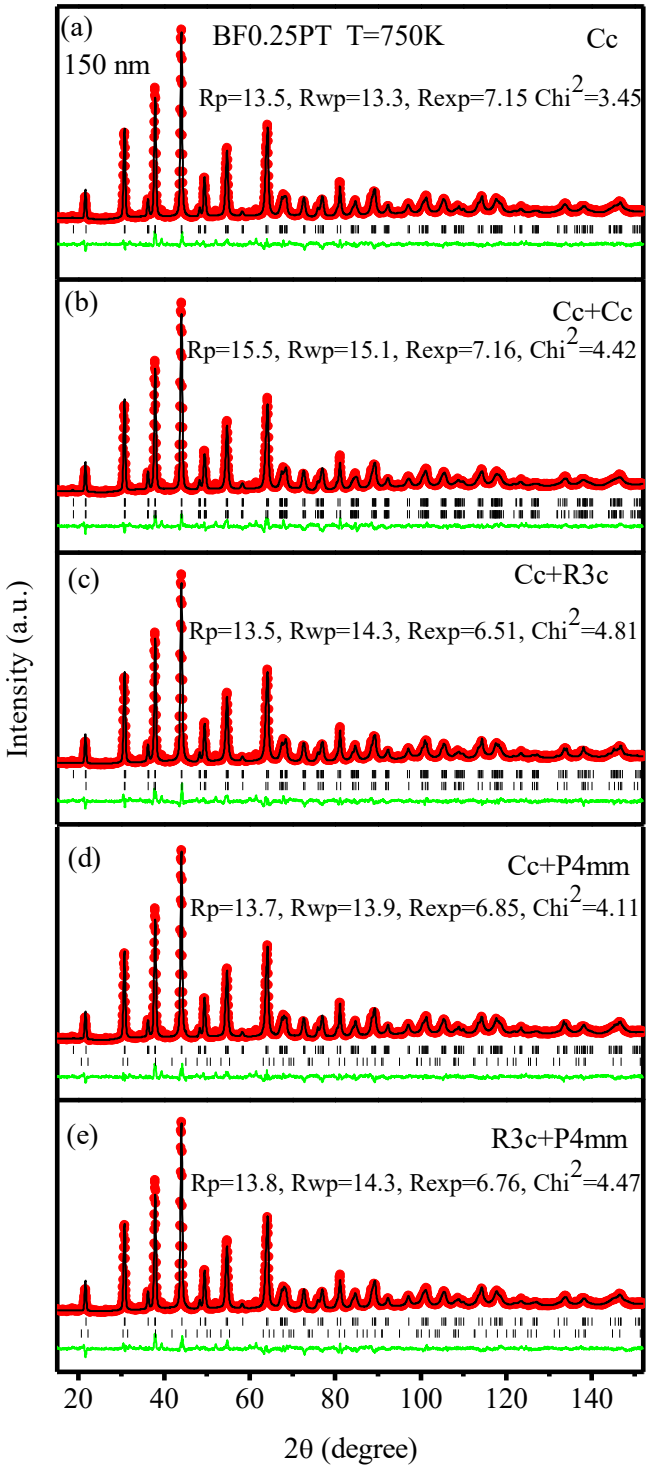

Fig. 5.1 Rietveld refinement profile for different structural models (a) Cc (b) Cc+Cc (c) Cc+R3c (d) Cc+P4mm and (e) R3c+P4mm of neutron powder diffraction pattern taken at 750K for 150nm size BF-0.25PT.

5.4.2 Magnetization studies of BF-0.25PT powder

The DC M(T) measurements were carried out at 500Oe from 300K to 900K.Fig.5.2 shows the M(T) plot for the samples with particle sizes 2μm, 500 nm, 300 nm and 150 nm. These plots clearly reveal a peak corresponding to the antiferromagnetic transition. The Néel transition temperature (T_N) was determined from the derivative plots of the M(T) curves in the vicinity of the peak temperature. The 2μm size powder, which we shall treat as representative of the bulk behavior shows T_N at 445K. Below the T_N, there is another transition, which is better revealed in the derivative plot (inset of fig 5.2a). This transition is known to be due to spin reorientation transition in bulk BF-0.25PT [Bhattacharjee et al .(2013)].

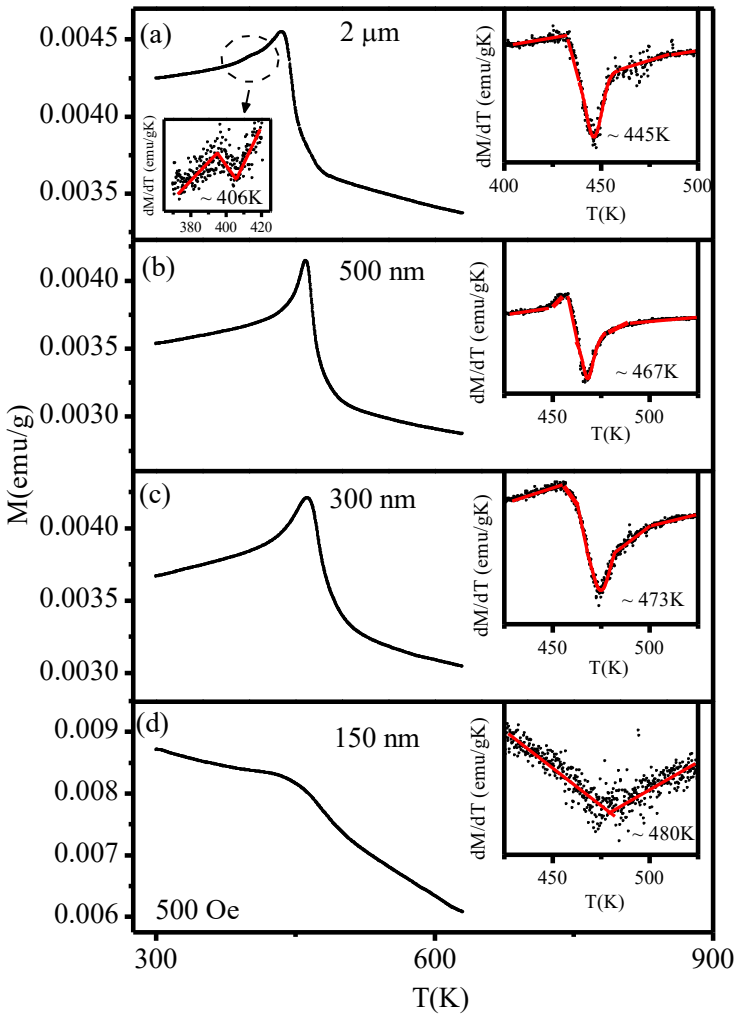

Fig. 5.2 Temperature dependence of field heating (FH) magnetization (M) for (a) 2µm (b) 500 nm (c) 300 nm and (d)150 nm BF-0.25PT sample.

On decreasing the particle size below 2µm, the signature of spin reorientation transition disappears. As a result, the AFM peak in the M(T) plot for 500 nm size powder becomes relatively sharper than that for 2µm powder (compare Fig 5.2 (a) and (b)). However, on decreasing the particle size further, the AFM transition peak shows rounding and smearing (see Fig. 5.2 (c) and (d)). The 150nm size powder infact shows very broad peak around T_N. This broadening is not induced by $PbTiO_3$disorder which is fixed at x=0.25

but is essentially a signature of the finite size effect [Binder et al. (1972)]. On decreasing particle size below 150 nm, the tetragonal phase starts appearing and hence our study of the finite size effect in the monoclinic phase was restricted upto 150nm size powders only. When the tetragonal and monoclinic phases coexist, the situation become more complex as these phases can also form a core -shell structure in the same particle. The most remarkable feature of the M(T) plots in Fig 5.2 is the increasing trend of T_N with decreasing particle size. This is in marked contrast to the situation in pure BF where on decreasing the particle size, T_N was shown to decreases as per the predictions of the Scaling theories [Lang et al. (2006)].

As the M(T) plot shows a rather broad peak around T_N for 150 nm size powder, the T_N was cross-checked using neutron scattering measurements also for this smallest size. Fig. 5.3(a) depicts the evolution of neutron diffraction pattern of the 150 nm size powder in a limited 2θ range for temperatures from 300 to 600K. The first peak at ½ ½ ½ pseudocubic position in these patterns, marked by an arrow, is the characteristic antiferromagnetic peak. The variation of the integrated intensity of this peak with temperature is depicted in fig.5.3(b). It is evident from this figure that the intensity of the antiferromagnetic peak decreases on increasing the temperature above 300K almost linearly. This is expected, as the intensity of the antiferromagnetic peak is proportional to the square of the order parameter. Above about 500K, the intensity follows a different slope with considerably reduced value. The remanent intensity above 500K is due to the presence of short-range antiferromagnetic correlations above T_N as well as the presence of a nuclear peak due to the Cc space group with rather low intensity. Most interestingly, the slope of the linear plot changes around 480K which corresponds to the T_N for the 150 nm size sample

determined by M(T) measurements. This provides an independent confirmation of the transition temperature determined by M(T) measurements.

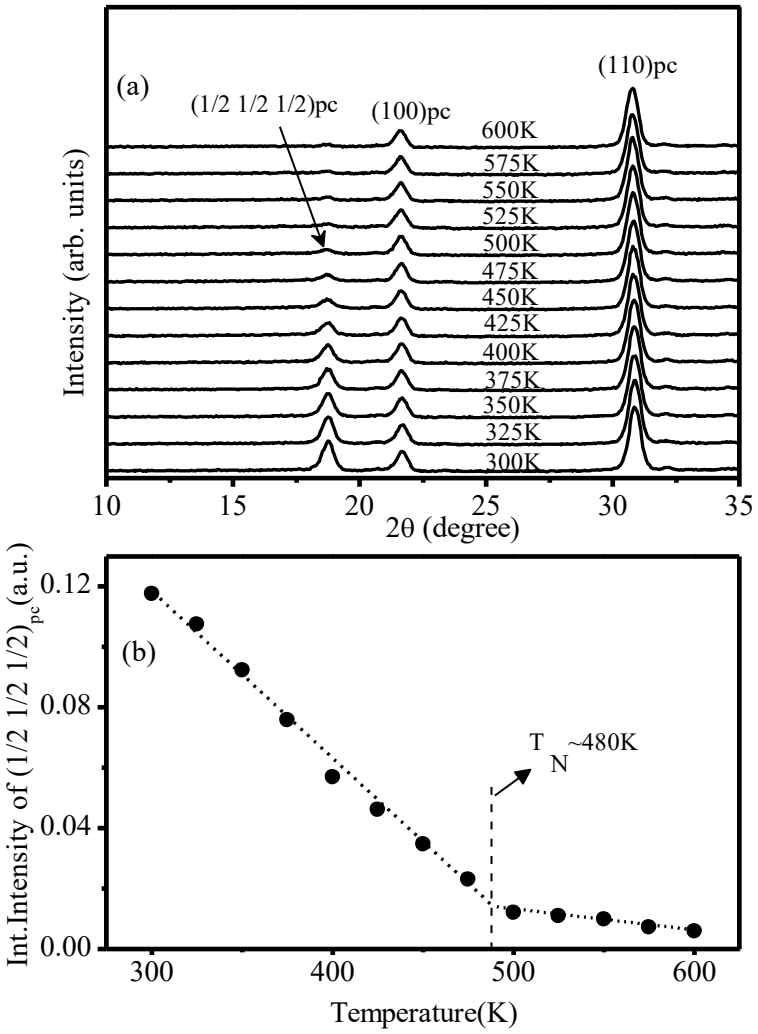

Fig. 5.3 (a) Temperature dependent neutron profile of BF-0.25PT in the low 2θ region (b) Integrated intensity of first magnetic peak of sample BF-0.25PT of size 150nm.

5.4.3 Effect of particle size on spin reorientation transition

The monoclinic compositions of BF-xPT have been shown to undergo a spin reorientation transition below the Néel temperature. The magnetic transitions have been described in the following manner by Bhattacharjeeet al (2013) with decreasing temperature:

Paramagnetic $\xrightarrow{T_{OPT}} \Gamma_2^{001}(G^yF^{xz}) \xrightarrow{T_N} \Gamma_1^{000}(G^{xz}F^y)$, where $\Gamma_2{}^{001}$ and $\Gamma_1{}^{000}$ are the irreducible representations (Irrep) of the magnetic Fe sublattice (4a Wyckoff site) forpropagation vectors k = 0,0,1 and 0,0,0 while G^yF^{xz}; $G^{xz}F^y$ present the magnetic structure in Bertaut notation corresponding to the two Irreps. In the Bertaut notation, G and F stand for AFM and FM components while the superscripts denote the direction (x/y) or plane (xz/xy) of magnetisation.

The M(T) plot for 2 μm sample reveals both the Néel temperature (T_N) and spin reorientation temperature (T_{OPT}) are 445 K and 406K, respectively (see Fig. 5.2(a). However, on decreasing the particle size, there is no evidence of the spin reorientation transitions in the M(T) plots. Since the reduction in particle size leads to the rounding and smearing of the AFM transition peak in M(T) (see Fig. 5.2(c) and (d)), it is likely that the weak anomaly at the spin reorientation temperature is getting masked by particle size broadening. In order to verify the presence or otherwise of the spin reorientation transition, we carried out Rietveld refinement of the magnetic structure using the neutron powder diffraction data at 450K, a temperature just below T_N but above the bulk spin reorientation transition temperature T_{OPT}, using all the possible Irreps, i.e. $\Gamma_1{}^{001}$ and $\Gamma_2{}^{001}$ belonging to k = 0,0,1 and $\Gamma_1{}^{000}$ and $\Gamma_2{}^{000}$ belonging to k=0,0,0 as discussed by Bhattacharjeeet al (2013). The results are shown in Fig. 5.4. The values of χ^2 and R_{mag} belonging to each model have been given in this figure. Evidently, the Irrep$\Gamma_1{}^{000}$ gives the

best fit amongst all the possible models indicating that the magnetic structure at this temperature belongs to the $\Gamma_1^{000}(G^{xz}F^{y})$ Irrep.

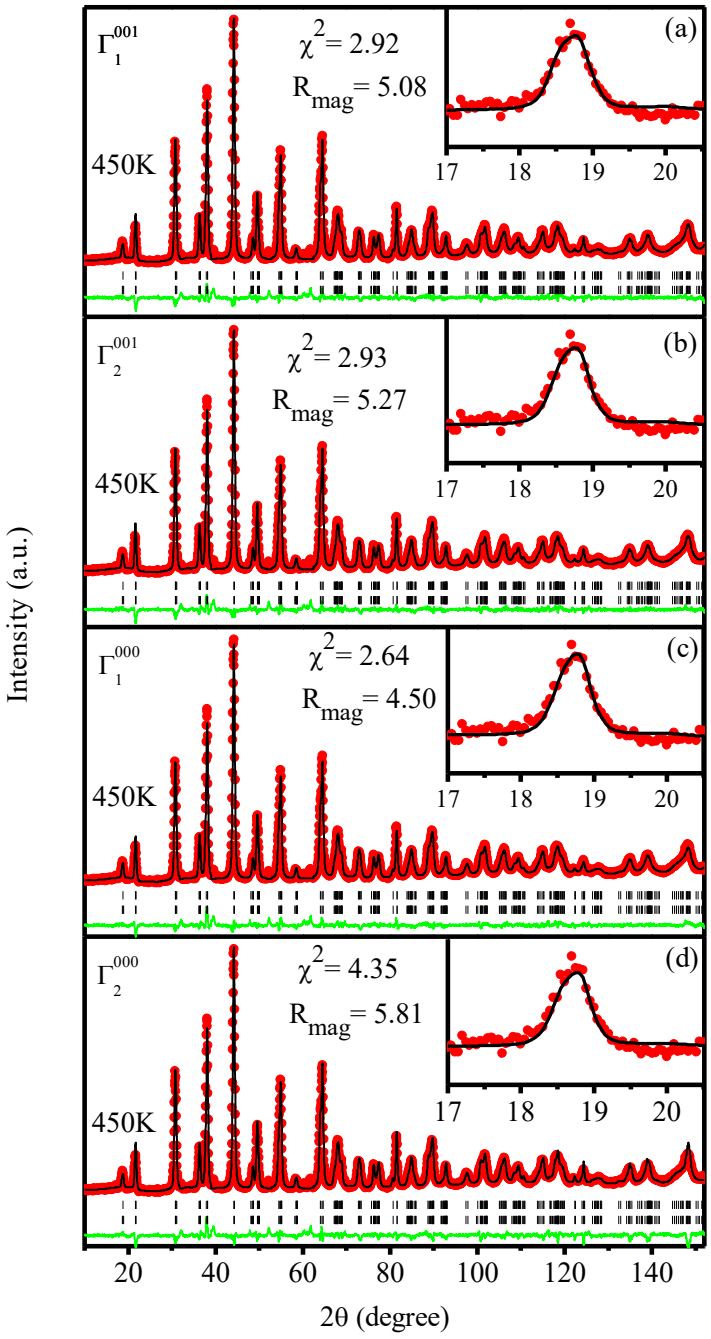

Fig. 5.4 Rietveld refinement of the magnetic structure using the neutron powder diffraction data at a temperature 450K using all the possible representations.

At room temperature (300K) also (i.e. below T_{OPT}), the Irrep Γ_1^{000} gives a better fit with lower χ^2 Bhattacharjee et al. (2013). The Irrep Γ_2^{000} leads to an inferior fit with higher χ^2. Figs. 5.5 (a) and (b) show the Rietveld fits for 150 nm sample at 300K using the Irreps Γ_1^{000} and Γ_2^{000}, respectively. The refined parameters obtained for 300 K and 450 K are given in table 5.2. On the basis of the refinements using neutron powder diffraction data, we may conclude that the spin reorientation transition does not occur in the nanoparticles, as indicated by M(T) plots also. This is another feature of size reduction in the monoclinic compositions of BF-xPT for $x < 0.27$. Thus,the nanoparticles having the size of 150 nm undergo paramagnetic to G type AFM ordering, with spin configuration belonging to the Irrep $\Gamma_1^{000}(G^{xz}F^{y})$, directly without the intermediate structure reported for bulk by Bhattacharjee et al. (2013).

We also analysed the temperature dependence of the orderedmagnetic moment per Fe atom. This is shown in fig. 5.6. It is evident from the figure that the ordered moment drops rapidly upto ~473K, but does not vanish completely until the temperature reaches 700K. The temperature dependence of the ordered moment was fitted to a power law, $\mu = \mu_0 [(T_N - T)/T_N]^{\beta}$, which gives the value of $\beta=0.346$. This value differs from the β value (½) expected for the molecular field theory and Landau theory of second order phase transition. This value of β is close to the value of the critical exponent 1/3obtained for spin-wave theory and Callen decoupling Eibschütz et al. (1967), Patel et al. (2013) and has been reported in orthoferrites as well as BF solid solutions [Bhattacharjee et al. (2010)].

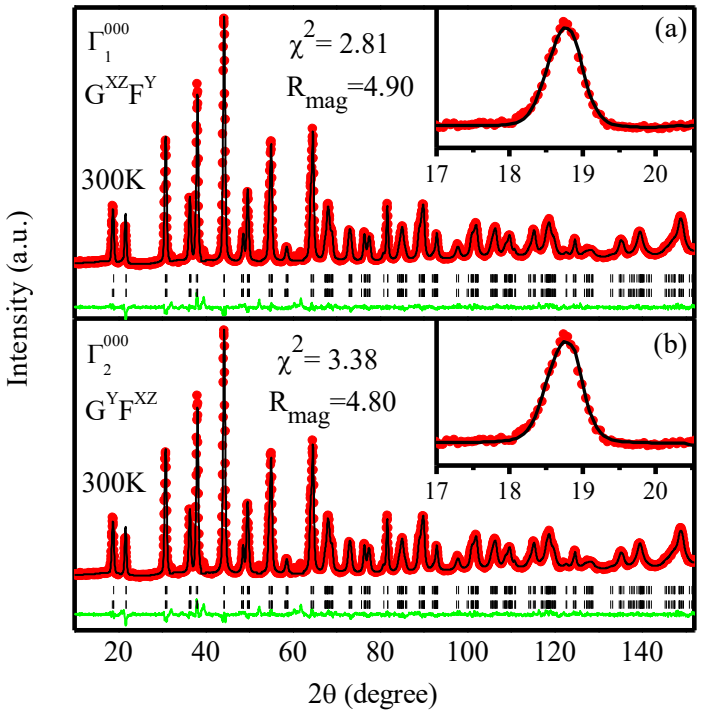

Fig. 5.5 Rietveld refinement of the magnetic structure using the neutron powder diffraction data at a temperature 300K using all the possible representations.

Table 5.2 Refined structural parameters of BF-0.25PTusing Cc space groupas obtained from neutron powder diffraction.

BF0.25PT ofsize 150 nm at different temp.		**Fractional coordinates**				**Thermal Parameters (Å^2)**	**Lattice Parameters (Å)**	**Statistical parameters**
		Atom	**x**	**y**	**z**			
300K	**Cc**	Bi/Pb	0.0	0.25	0.0	B_{iso}=1.12(3)	a=9.7846(1) b=5.5835(8) c= 5.6244(7) β = 125.66(5)	R_p= 7.72 R_{wp}= 8.91 R_{exp}= 5.31 χ^2 = 2.81 Magnetic R-factor: 4.9
		Fe/Ti	0.281(1)	0.256(4)	0.745(4)	B_{iso}=0.51(5)		
		O1	0.041(2)	0.306(9)	0.461(2)	B_{iso}=0.93(1)		
		O2	0.321(1)	0.489(6)	0.024(3)	B_{iso}=0.78(7)		
		O3	0.279(2)	-0.026(5)	-0.051(6)	B_{iso}=1.15(4)		
450K	**Cc**	Bi/Pb	0.0	0.25	0.0	B_{iso}=1.65(1)	a=9.8016(1) b=5.5928(2) c= 5.6294(3) β = 125.65(1)	R_p= 8.86 R_{wp}= 9.52 R_{exp}= 5.72 χ^2 = 2.64 Magnetic R-factor: 4.5
		Fe/Ti	0.280(1)	0.250(4)	0.744(7)	B_{iso}=0.84(1)		
		O1	0.039(8)	0.308(4)	0.458(1)	B_{iso}=1.21(1)		
		O2	0.317(1)	0.495(1)	0.018(6)	B_{iso}=1.21(6)		
		O3	0.276(4)	-0.021(7)	-0.048(6)	B_{iso}=1.59(1)		

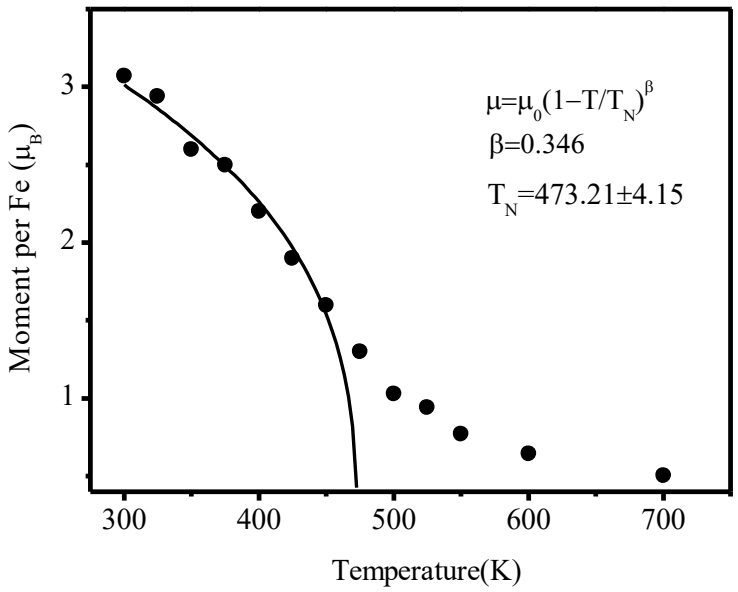

Fig.5.6 Magnetic moment (filled circles) obtained from the Rietveld refinements using the neutron powder diffraction data along with the fitted curve for $\mu = \mu_0 [(T_N - T)/T_N]^{\beta}$.

5.4.4 Role of crystal-chemical parameters in enhancing T_N

The FE, FM and AFM transition temperatures (T_C) are known to decrease with decreasing particle size below a critical size. This decrease in transition temperature has been explained in terms of the scaling theories which relate the particle size (d) and the correlation length (ξ) with the T_C in the following manner [Binder et al. (1972).

$$\frac{T_C^b - T_C^{grain}}{T_C^b} = \left(\frac{d}{\xi_0}\right)^{-(1/\nu)} \qquad (5.1)$$

where T_C^b and T_C^{grain} are the bulk and finite size transition temperatures, d is the grain diameter, ξ_0 is the magnetic correlation length at 0K and ν the critical exponent related to ξ.

Thus, any increase in T_N with decreasing particle size is rather unusual and calls for an explanation. We had earlier shown a huge enhancement of T_N as a result of particle size reduction in a tetragonal composition of BF-xPT taking x=0.50 (BF-0.50PT) as example.

In case of BF-0.50PT nanoparticles, there is an increase in the Néel temperature from 120K for bulk to 350K for18 nm size particles. The increase in case of monoclinic BF-0.25PT is rather modest(T_N~445K for bulk to 480K for150 nm size particles). This difference in increase in T_N with decreasing size in tetragonal and monoclinic compositions also calls for an explanation. The huge enhancement of T_N in tetragonal BF-xPT was explained by us in terms of the reduction in the ferroelectric distortion leading to shortening of the longer Fe-O bond length along the [001] direction. As a result of such a shortening of the longer Fe-O bond length, the strength of the superexchange interaction increases leading to an increases of the T_N (discussed in chapter IV). This longer Fe-O bond length is much larger than the sum of the ionic radii of Fe^{3+} and O^{2-} as a result of which the superexchange interaction pathways are along [001] are nearly broken and AFM state of BF-0.50PT in bulk is essentially 2-dimensional (2d). Thus, the increase in T_N with decreasing particle size in the tetragonal phase of BF-xPT is essentially linked with a crossover from nearly 2d AFM ordering in bulk due to broken super exchange pathways in the [001] direction to a 3d AFM ordering in smaller particles due to reestablishment of superexchange interactions in this direction as a result of the reduced ferroelectric distortion. However, in the monoclinic composition of BF-0.25PT, none of the bonds is actually too large like BF-0.50PT and as such the exchange pathways are not completely broken. What is even more intriguing in case of BF-0.25PT is that the particle size dependence of T_N in this system is opposite to that of pure BF. In pure BF, T_N decreases with particle size as per the scaling law of Eq (5.1). [Selbach et al.(2007)]

To understand the effect of particle size on T_N in BF-0.25PT, we first present a comparison of the various Fe-O bond lengths, which decide the exchange pathways, for

the bulk and nanocrystalline monoclinicBF-0.25PT, as well as and bulk rhombohedral BF as shown in Fig. 5.7(a) and (b).

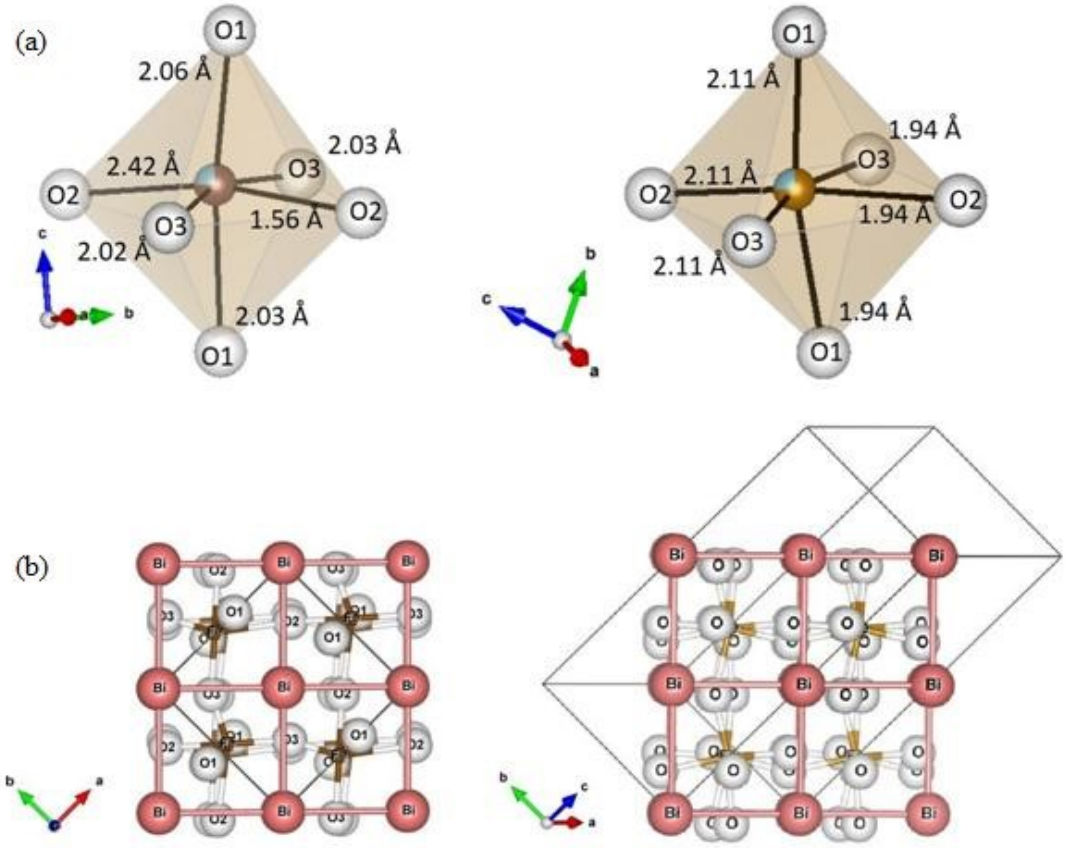

Fig. 5.7 (a) The Fe-O bond lengths for the octahedral coordination in monoclinic BF-0.25PT and rhombohedral $BiFeO_3$. (b) Comparison of asymmetry of bond lengths for BF-0.25PT and $BiFeO_3$.

The structural parameters obtained from Rietveld analysis of the SXRD were used to calculate the bond lengths and bond angles for Fe-O linkages belonging to the oxygen octahedron. The parameters so obtained are listed in Table 5.3. In the ideal perovskite structure, all the Fe-O bonds of the octahedron are equal and O-Fe-O bond angles are 180^0. As a result of ferroelectric distortion, one observes unequal Fe-O bond lengths and

deviation from 180^0 bond angle. Corresponding to the three oxygen atoms, O1, O3 (both planar oxygen) and O2 (apex oxygen), in the asymmetric unit, there are three pairs of Fe-O bond lengths and three O-Fe-O angles different from 180°. The results of Rietveld refinement reveal a systematic change in the bond angles and bond lengths of the apex oxygen atoms. We define an asymmetry parameter as a measure of the deviation in the bond length from the ideal perovskite oxygen octahedra as a ratio of the difference in the two opposite bond lengths to the sum of these opposite bond lengths as given below

$$\% \text{ Asymmetry (Asym)} = \frac{((Fe-O)_I-(Fe-O)_{II})}{((Fe-O)_I+(Fe-O)_{II})} X100$$

Table 5.3 Details of bond length and bond angle of BF-0.25PT of different sizes and bulk $BiFeO_3$ [Goswami et al (2011)].

Size (nm)	Bond length (Å)		Asym (%)	Bond length (Å)		Asym (%)	Bond length (Å)		Asym (%)	Bond Angle (°)		
BF-.25PT	$(Fe\text{-}O1)_I$	$(Fe\text{-}O1)_{II}$		$(Fe\text{-}O2)_I$	$(Fe\text{-}O2)_{II}$		$(Fe\text{-}O3)_I$	$(Fe\text{-}O3)_{II}$		O1-Fe-O1	O2-Fe-O2	O3-Fe-O3
2000	2.06(5)	2.03(5)	0.73	2.42(5)	1.56(5)	21	2.02(5)	2.03 (5)	~0	163.1(5)	151.4 (6)	166.5 (7)
500	2.13(5)	1.96(5)	4.15	2.37(5)	1.48(5)	23	2.07(5)	2.08 (3)	~0	162.0(6)	149.1 (7)	159.0 (6)
300	2.16(5)	1.94(5)	5.36	2.37(5)	1.49(4)	23	2.07(5)	2.09 (4)	~0	160.3(5)	146.3 (7)	157.8 (6)
150	2.21(5)	1.89(3)	7.80	2.47(6)	1.63(3)	21	2.01(7)	1.96(3)	~0	160.4(1)	146.2(5)	155.3(4)
Bulk $BiFeO_3$	2.11(8)	1.94(9)	4.15	2.11(8)	1.94(9)	4.15	2.11(8)	1.94(9)	4.15	167.4(1)	167.4(3)	167.4(2)

It can be seen from Table 5.3 that the asymmetry parameter significantly increases for the Fe-O1-Fe bonds from0.73 for bulk to 7.8% for the nanocrystalline sample, while the asymmetry for the Fe-O2-Fe bonds increases from 21% to 23% only. The Fe-O3-Fe bond lengths remain nearly symmetric and unaffected by particle size reduction. The systematic increase in the asymmetry parameter on decreasing the particle size correlates well with the Néel temperature of the samples which increases from 445K for bulk to

480Kfor 150 nm size particles (see Fig. 5.8). Further, the change in the asymmetry parameter is much more prominent between bulk and 500 nm size particles than between 500 nm and300 nm particles. This is consistent with the change in the T_N which changes from445K for bulk to 467K for the 500 nm size powders and thenfrom473Kfor 300 nm size to 480 K for 150 nm.

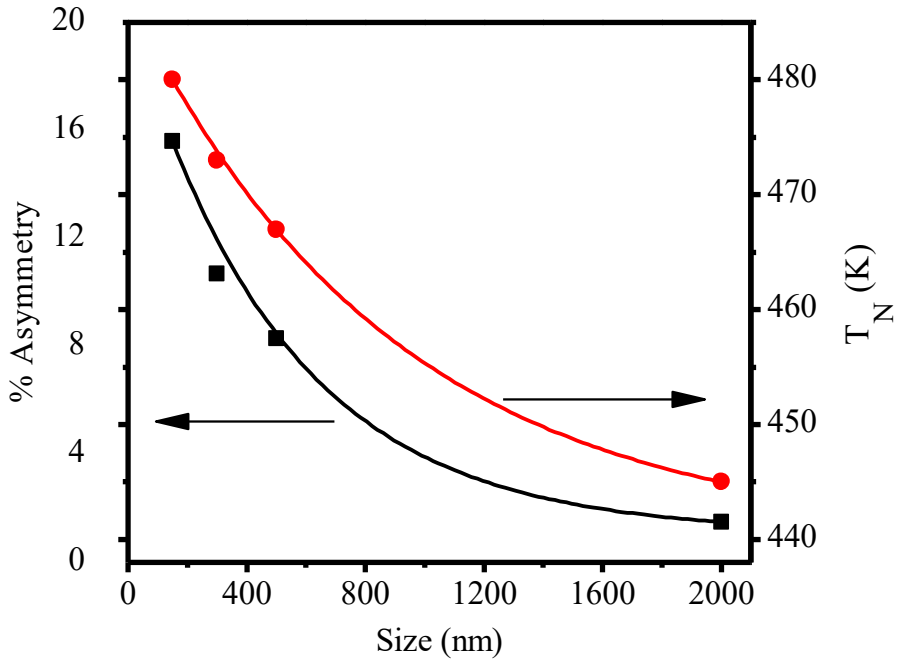

Fig.5.8 Variation of Neel temperature and percentage anisotropy with particle size of BF-0.25PT, highlighting their correlations.

The next question that arises is about the difference in the variation of the Néel temperature with particle size in rhombohedral $BiFeO_3$and monoclinic BF-0.25PT. While T_N of $BiFeO_3$follows the scaling theory [Selbach et al.(2007)], BF-0.25PT does not. The answer lies again in the structural details. In case of $BiFeO_3$, all the three Fe-O-Fe exchange pathways are equally asymmetric (see Table 5.3) for both bulk and nanocrystalline samples due to the rhombohedral space group R3c [Goswami et al. (2011)]. In contrast, in BF-0.25PT, the asymmetry parameter for the Fe-O1-Fe path way

increases significantly with decreasing particle size and correlates well with the Néel temperature (see Fig. 5.9). Further, there is only a small variation in the asymmetry parameter for Fe-O2-Fewith size while asymmetry parameter is nearly constant for Fe-O3-Fe. Thus, the bond asymmetry parameter captures the most significant difference between BF-0.25PT and $BiFeO_3$for the three super exchange pathways. This difference is depicted in Fig. 5.6(b) at the elementary perovskite unit cell level. The uniform asymmetry along all the three superexchange pathways can be clearly seen in case of $BiFeO_3$in the figure but not in case of BF-0.25PT. It is very likely that these differences in the asymmetry parameter trigger a unique behavior in the nanoparticles of BF-0.25PT solid solution.

As mentioned earlier, the increase in the Néel temperature is quite large in case of BF-0.50PT, 120K for bulk to 350K for 18 nm size particles, whereas it is comparatively much smaller for BF-0.25PT. The major difference in the Fe-O-Fe superexchange pathways of tetragonal BF-0.50PT, monoclinic BF-0.25PT and rhombohedral $BiFeO_3$ is highlighted in Fig.5.9. In case of BF-0.50PT,one of the Fe-O1 bond lengths in the z direction is significantly larger than the sum of the two ionic radii due to the ferroelectric distortion. As a result, the exchange pathway is broken in the z-direction and the nature of AFM ordering becomes essentially 2-d. When the size is reduced, the ferroelectric distortion also decreases which in turn reduces the longer Fe-O bond length in the z direction. With decreasing Fe-O bond length, the superexchange interactions grow along the z direction leading to a cross over from 2-d to 3-d AFM interactions and increase in T_N. In case of BF-0.50PT, there is considerable room for this manipulation of the Fe-O bond length along the z-direction and hence the strength of the superexchange interaction.

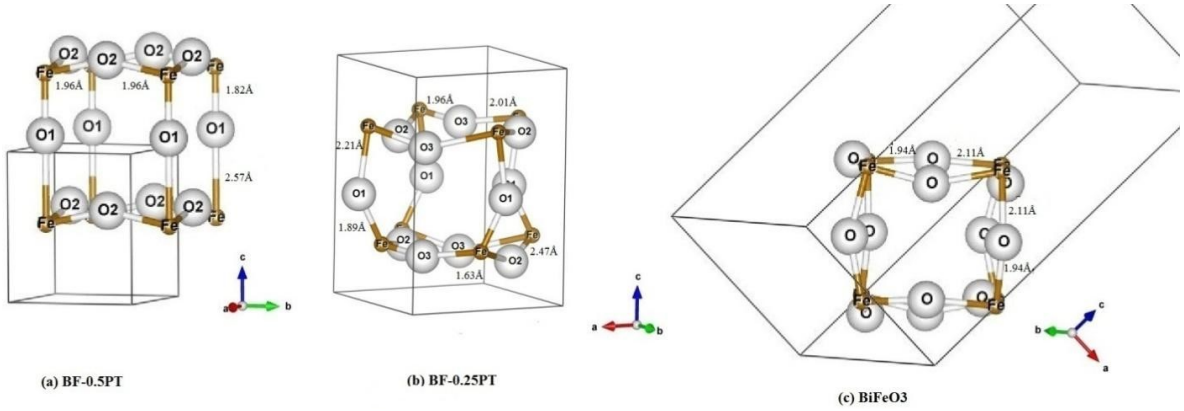

Fig.5.9 Fe-O-Fe exchange pathways (a) tetragonal $BiFeO_3$-0.50$PbTiO_3$, (b) monoclinic $BiFeO_3$-0.25$PbTiO_3$ and (c) rhombohedral $BiFeO_3$

This explains the large increase in the Néel temperature from 120K for bulk to 350 K for 18nm particles. In case of monoclinic BF-0.25PT, the Fe-O bonds are never broken in any direction due to the ferroelectric distortion and as a result there is comparatively much smaller change in the bond lengths due to size reduction. The superexchange pathways are already in the 3-d regime leaving less scope for manipulating the strength of the superexchange interactions through reduction in ferroelectric distortion with decreasing particle size. As discussed earlier, the increase in the asymmetry of the two Fe-O1 bond lengths with decreasing size in a particular direction seems to be playing the most significant role in deciding the strength of the superexchange interactions in case of BF-0.25PT. The asymmetry in the Fe-O bond lengths in case of $BiFeO_3$ is same in all the crystallographic directions irrespective of the size due to the rhombohedral symmetry in contrast to the previous two cases with tetragonal and monoclinic.

In Anderson's theory of superexchange interactions, the strength and nature of the interaction mainly depends on the overlapping integral of the participating ions, which in turn depends on the crystal field parameters Anderson (1950). So, in case of oxides where the magnetic ordering is getting facilitated through superexchange interactions, two physical parameters play very important role: the bond lengths in Fe-O-Fe and Fe-O-Fe bond angle. In case of tetragonal BF-0.50PT, only the bond length in c direction is affected by particle size, whereas size reduction strongly affects both the bond length and bond angle (see Table 5.3)in monoclinic BF-0.25PT.For such asymmetric superexchange interactions, an additional term $H_{DM} = D_{ij}\bullet(S_i \mathrm{x} S_j)$, where $D_{ij}$is the Dzyaloshinskii vector, needs to be considered in the main Hamiltonion Moriya (1960). For large asymmetries, the Dzyaloshinskii-Moriya(DM) interaction term cannot be ignored. We believe that it is this DM interaction term that may be responsible for increase in T_N with decreasing particle size in case of monoclinic BF-0.25PT.

5.5 Summary and conclusions

1. The Néel transition temperature (T_N) of BF-0.25PT increases from 445K for bulk to 480 K for 150 nm particle size using magnetization and neutron powder diffraction data. Based on Rietveld refined structural parameters, we show that the asymmetry and non-linearity of the Fe-O-Fe superexchange pathways grows with decreasing particle size and that they exhibit a strong correlation with T_N. We believe that thesubstantially enhanced Dzyaloshinskii-Moriya (DM) interaction with decreasing particle size as a result of asymmetric and non-collinear Fe-O-Fe superexchange pathways may be the key factor in raising the T_N on decreasing the particle size.

2. It has been established that the spin reorientation transition occurring below T_N in bulk monoclinic compositions like BF-0.25PT is suppressed in the nanocrystalline samples of ~150 nm particle size.

As it can be seen from the variation of integrated intensity of $(½,½,½)_{pc}$ peak with temperature shown in figure 5.3 and the variation of magnetic moment with temperature as shown in figure 5.6, there is a non-zero value persists even at temperature above the Neel transition temperature. We have investigated this peculiar behaviour as described in the chapter VI.

.